Tunability and sensitivity investigation of MREs in longitudinal vibration absorbers

A Thesis
Presented to
The Academic Faculty

by

Anne-Marie Albanese Lerner

In Partial Fulfillment
of the Requirements for the Degree
Doctor of Philosophy

School of Mechanical Engineering
Georgia Institute of Technology
December, 2008

Tunability and sensitivity investigation of MREs in longitudinal vibration absorbers

Approved by:

Dr. Ken Cunefare
School of Mechanical Engineering
Georgia Institute of Technology

Dr. Christopher Lynch
School of Mechanical and Aerospace Engineering
University of California Los Angeles

Dr. Nader Sadegh
School of Mechanical Engineering
Georgia Institute of Technology

Dr. Reginald DesRoches
School of Civil and Environmental Engineering
Georgia Institute of Technology

Dr. Massimo Ruzzene
School of Aerospace Engineering
Georgia Institute of Technology

Date Approved August 14 , 2008

To my parents, who have guided me from the very beginning,

To Micah, who has been the inspiriation to finish,

and to Dan, who was with me every step of the way,

I could never have done any of this without you.

This work is for all of you.

ACKNOWLEDGEMENTS

I would like to thank Dr. Kenneth Cunefare, my mentor and advisor, for introducing me to the field of semiactive control, and guiding me through this dissertation process. To my committee members, Dr. Christopher Lynch, Dr. Massimo Ruzzene, Dr. Nader Sadegh, and Dr. Reginald DesRoches, thank you for your guidance, assistance, and patience. I would also like to thank Dr. Ginsberg for mentoring me as I taught my first course. The wonderful people at UW-Rock County have been incredibly patient as I've finished up my dissertation; thank you to Dean Diane Pillard, Bob McCallister, Jon Fons, Jack Champeau, Dale Buechler, and Grace Ni for your support. To the women of WSGW and especially Janine Johnson, thank you for your friendship, sympathy, and encouragement through this process. My labmates, especially Mark Holdhusen, who told me what I needed to hear to finish, and Jeff Badertscher for his invaluable assistance and editting remarks , and Alex Michaud, who kept me in good humor, have been especially valuable. Finally, I would like to thank my wonderful family, who have supported me through this entire endeavour.

To all of you, thank you.

TABLE OF CONTENTS

LIST OF FIGURES

SUMMARY

Broadband, variable, and random excitations are often suppressed using active vibration absorbers (AVAs). While AVAs can be effective, they also are expensive and subject to instability when the disturbance is ill defined. A state-switched absorber (SSA) can be used for these same vibration classes while reducing the expense and instability because an SSA is only allowed to be active at discrete instances. SSAs are spring-mass-damper devices in which at least one element is controllably variable. The work presented in this dissertation evaluates the properties of magnetorheological elastomers (MREs) to assess their use in SSAs as variable springs.

MREs are elastomers doped with magnetically permeable material, generally iron. They are modeled as lossy springs, and have stiffness and loss factor components. Natural frequency and stiffness behavior, and their relationships to static displacement, iron content, and forcing frequency and amplitude were determined. Loss factors were found to be independent of MRE content, configuration, and static displacement. This was confirmation that MREs are in fact controllable springs. Natural frequencies changed in the presence of magnetic fields by as much as 360%. The corresponding change in static displacement could not account for this frequency change.

Transient data was found by determining the length of time it took for an MRE to achieve quasi-steady state oscillation behavior when subjected to a harmonic excitation. This time was referred to as the characteristic response time. The characteristic response time correlated to the ratio of the forcing frequency to the zero-field natural frequency. When a magnetic field was turned on, the characteristic response time on average was found to be consistently longer than when the magnetic field was turned off, regardless of iron content or configuration. The difference between these two characteristic response times is caused by the particles' mechanics. To form a chain, a magnetic field must both be set up, and particles must move to join together. When a chain is broken, the magnetic field

must merely be removed. However, this difference gives opportunities for future research to be conducted on controlling MREs' transient responses.

CHAPTER I

INTRODUCTION

Magnetorheological elastomers (MREs) are heterogeneous materials consisting of ferromagnetic particles dispersed in chain-like patterns within elastomeric matrices. Because MREs contain ferromagnetic particles, their stiffness have been found to increase in the presence of magnetic fields [7]. Due to their stiffness changing properties, MREs are a subject of interest particularly for vibration control applications. MREs can be implemented as active vibration suppression elements within vibration absorbers [17]. The work presented here investigates the transient behavior of MREs contained in longitudinal vibration absorber configurations and their controllability and stability limits, with an emphasis on their ability to operate as state-switched absorbers (SSAs).

MREs were used as the subject of study because their Young's and shear moduli are magnetic-field dependent (see Chapter II for a thorough discussion of this subject). This means that when placed in series with a mass, MREs behave as variable-stiffness springs. Due to the curing methodology employed to create MREs, discussed in more detail in Section 2.2, the MREs' behavior is dependent upon the orientation of the excitation with respect to the magnetic field.

For the research discussed in this dissertation, MREs were excited parallel to the direction of their internal chains, which is referred to as "longitudinal" excitation. This is contrary to what has been done previously by many researchers, which was to implement MREs in vibration absorption applications such that the magnetic field was perpendicular to the direction of excitation [40, 33, 23, 16, 10]. Exciting MREs in this configuration is commonly referred to as "shear" excitation. Original MRE work contained MREs in the shear excitation configuration because the theory behind MREs' behavior in this configuration was well-understood, as will be detailed in Section 2.1. However, recent studies have found that MRE excitation parallel to the direction of magnetic field can produce larger

stiffness changes than excitation in the shear orientation [2].

MREs were studied with the goal of use within an SSA device. SSAs, which are discussed in Section 2.1, have a specific tuning algorithm that requires a switchable spring to change from state to state "instantaneously". In practical terms, this means that state switching must be complete within a quarter-cycle of the frequency of interest to maintain stability [20]. While MREs are known to exhibit stiffness changes in the presence of changing magnetic fields, the time-dependent behavior of these changes have not been studied. The purpose of this dissertation were to answer the questions "how do micro scale MRE models predict to macro scale MRE behavior?" and "what are the transient properties of these MREs for purposes of SSA control?" Four research objectives were developed to answer these questions. These objectives were to:

- create a numerical model describing micro scale MRE behavior
- use the micro scale numerical model to predict macro scale MRE behavior
- assess stability and controllability properties
- determine the transient behavior of MREs in longitudinal excitation

A two-dimensional micro scale numerical model was developed so that known information, such as the host elastomer's stiffness and the filler particle's nominal diameter, could be synthesized to predict aggregate MRE behavior in a vibration absorber configuration. FEA packages on the market require prior knowledge of MRE behavior (stiffness, loss factor, damping, etc.) in order to predict knowledge in future configurations. The micro scale numerical model developed for this research does not require prior knowledge of MRE behavior, just knowledge of the separate elastomer and particulate properties.

The micro scale MREs were modeled as very small portions of MRE elastomers. Each individual portion was treated as a block, which could be built upon to create a two-dimensional face. The effects of building up, or scaling, on predicted property behavior was compared to known property behavior recorded from experimental tests. Knowledge

of how properties' predictions are affected by scaling can be used in future to extrapolate future properties from small-scale MRE modeling in this manner.

Simulation results from these micro scale MREs were put into context of full-sized MREs by treating each small simulation MRE as a building block, and building up larger MREs. Simulation results were compared to the original micro scale size as these MREs were "scaled up". The pattern of predicted behavior was extrapolated as a function of further scaling to predict MRE behavior at the macro scale, or full-sized MRE scale.

Stability and controllability properties were assessed in micro scale simulation and experimental MRE results. In order for an MRE to function as a switchable spring in an SSA, properties such as stiffness and loss factor, and each of these values' responses to changes in magnetic field must be understood. These properties are characterized in micro scale simulations, scaled up to predict macro scale response, and compared to experimental results.

Transient response of MREs to step changes in magnetic field was studied so that MRE behavioral dynamics could then be incorporated into an overall control algorithm to achieve successful SSA control. Stability and controllability limits must be assessed to ensure the successful SSA algorithm controls within the physical limitations of MRE behavior. It was anticipated that with this knowledge, engineers will have more complete information with which to design not only SSAs, but other AVA applications using MREs as a switchable spring.

The objectives were achieved through a combination of experimental and numerical research. A simulation was developed, as were methods for analyzing the simulation results, as described in Chapter III. Experimental methods and procedures are explained in Chapter IV. Static MRE properties, including stiffness and loss factors, found in the experimental data and simulation results are reported in Chapter V. Transient responses are evaluated in Chapter VI. Loss factors are reported in Chapter VII. The results reported in Chapters V and VI are synthesized to create a model describing MRE behavior and was tested for controllability and stability in Chapter VII, and numerically validated in Chapter VIII. Conclusions drawn from this research are presented in Chapter IX.

This research represents an advancement for AVA and SSA developers. The creation of this transient model gives developers a predictive tool to evaluate the usefulness of an MRE for their particular applications. This includes the frequency limitations of MREs when designing SSAs and AVAs, as well as physical limitations on its ability to respond to control inputs.

The subject of this dissertation was studied after a thorough investigation of the current state of research in the area of vibration absorbers, MREs, magnetic fields, and elastomer behavior modeling. The next chapter is dedicated to the discussion of tuned vibration absorbers (TVAs), adaptive tuned vibration absorbers (ATVAs), and state switched absorbers (SSAs), their uses, advantages, and disadvantages. Descriptions of smart materials used in ATVAs are also discussed. MREs in particular are discussed, including analytical and empirical models that have previously been established. Descriptions of other, magnetically manipulated devices are also discussed as well as their physical models. Previous research conducted by the author on the subject of MREs is included, as well as a discussion of the understanding of MRE behavior to date.

CHAPTER II

BACKGROUND

Vibration absorbers are devices that, when attached to base structures, minimize the base structure's vibration response to an excitation. Vibration absorbers can be "tuned" by selecting specific mass, damping, and stiffness values to minimize base motion at particular frequencies. Section 2.1 discusses TVAs as well as their active and hybrid vibration absorber (HVA) counterparts. AVAs, HVAs, and SSAs require "smart" materials, materials which possess characteristics that are controllable through an external stimulus. MREs are a class of smart materials, described in Section 2.2. MREs are comprised of elastomeric host matrices with embedded ferromagnetic particles. Section 2.3 discusses common elastomeric models and Section 2.4 covers the various ways magnetic fields have been modeled in the context of MREs.

2.1 TVAs, AVAs, and HVAs

Figure 2.1 depicts an example of a TVA, which is a spring-mass-damper devices. The TVA was developed in 1911 for suppression of vibration in ships, buildings, and aircraft [13]. TVAs were further developed to suppress vibration in rotating machinery, camshafts, multiple and single degree of freedom systems, and continuous systems [11]. TVAs can also control nonlinear systems as well as systems subject to random vibration excitation [28].

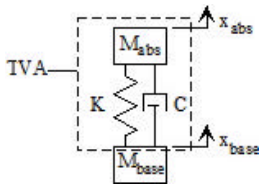

Figure 2.1: A TVA attached to a base mass.

While TVAs are very effective for a wide variety of applications, a TVA's performance is compromised in order to achieve effective attenuation over broadband or variable frequency

ranges [35]. Several alternatives to TVAs have been developed, including adaptive tuned vibration absorbers (ATVAs), AVAs, HVAs, and SSAs. These devices have been developed for use in different applications, although their fundamental construction was similar.

Since TVA performance is decreased in the presence of broadband, variable, or simply ill defined or unknown excitation [35], a different absorber was developed to control these types of excitation. A direct control AVA controls these excitations by imposing a force directly onto the vibrating mass. An indirect control AVA applies a force to the vibrating mass through a mass-spring-damper mechanism, where one or more of the spring-mass-damper elements can instantaneously and continuously change its properties to minimize vibration. Work on AVAs began using the direct control method, and AVAs were shown to outperform TVAs in broadband applications [29]. However, direct control AVAs can require significant amounts of energy, and therefore indirect control AVAs were developed. Furthermore, indirect control AVAs are much more closely related to TVAs and ATVAs. While indirect control AVAs are not necessarily an advantage over direct control AVAs, a device that has the capacity to function as an ATVA may also have characteristics that would lend itself to effective AVA application. Any future mention of AVAs in this dissertation implies an indirect control AVA.

While AVAs can be highly effective, they also pose the serious risk of adding energy to the overall system, leading to instability [1]. A disturbance must be either well defined, or very accurately measured to be able to implement this type of vibration absorber. AVAs are considered to be high-cost and high-risk, but very important to the development of helicopter rotors, flexible aerospace vehicle bending control, and isolating fighter pilots from their aircraft's motion [24], among other applications.

Hybrid vibration absorbers (HVAs) have been developed as a hybrid of the stable TVA and the adaptive AVA. HVAs can be significantly more robust than AVAs, while at the same time achieving vibration control that rivals the AVA [24]. An HVA is only permitted to change one or more properties at discrete and defined times. In between each property change, the HVA behaves as a passive TVA. An HVA can not add energy into the system, which minimizes the instability risk.

There are several types of HVAs, but for this work the focus is on adaptive tunable vibration absorbers (ATVAs) and state-switched absorbers (SSAs). An ATVA is generally used to control a system that was not well defined, such as a machine whose natural frequency is not known but operates at a constant frequency [35]. An ATVA is a device whose properties change quasi-statically until an optimal property value is found. Once an optimal property value has been found, it stays at that value and behaves as a TVA. An SSA is used to control well defined but changeable excitation. An SSA is a device that switches between different element values, or "states", to minimize an overall cost function, such as base energy [9]. The HVA considered in this dissertation was developed for SSA control applications, and will eventually be used to further develop control algorithms established by Cunefare et al [9].

The control algorithm employed by Cunefare et al [9] consist of two conditions; one condition determines candidate switch points based on avoiding shocks in the system response, and the other condition determines whether a switch would minimize base energy. Both conditions must be satisfied in order for a switch to occur. The candidate switch points for a changeable spring are when the energy level in each spring state would be equal, or when

$$k_i x^2 = k_j x^2, \tag{2.1}$$

where x was the spring expansion from its equilibrium state and k_i and k_j are the stiffnesses for states i and j, respectively. At the instant when the stiffness switches, the displacement will stay the same. Therefore, in order to satisfy Equation 2.1, the spring may only switch stiffnesses when $x = 0$. The candidate switch point condition mandates a constant energy level in the switching element during the switch, which was a key concept addressed in Section 5.3. Whereas Equation 2.1 determines whether or not the point in time was a candidate switch point, whether or not the stiffness should be switched was determined by

$$k_{SSA}^{next} = \left\{ \begin{array}{ll} k_{SSA1} & \text{if} \quad \dot{x}_{base}(\dot{x}_{SSA} - \dot{x}_{base}) > 0 \\ k_{SSA2} & \text{if} \quad \dot{x}_{base}(\dot{x}_{SSA} - \dot{x}_{base}) < 0 \\ k_{SSA} & \text{if} \quad \dot{x}_{base}(\dot{x}_{SSA} - \dot{x}_{base}) = 0 \end{array} \right\}. \tag{2.2}$$

This equation comes from the effort to minimize kinetic energy at the time when there was no

potential energy [9]. This method has been shown to be more effective than passive devices for single degree-of-freedom cases as well as continuous systems [21], and additionally was stable provided that a switch was complete within 1/4 of the period of the highest frequency of interest[20].

The nonpassive devices, AVAs, HVAs, SSAs, and ATVAs, all have elements that are changeable. While mechanical switching implementations have been developed, recent work has focused on materials with switchable elements. There are several materials that have been researched and developed as changeable elements, but the emphasis for the dissertation work lies on magnetorheological elastomers (MREs) as tunable springs.

2.2 MREs

An MRE is a smart material whose effective stiffness increases in the presence of a magnetic field. MREs contain ferromagnetic particles suspended in an elastomeric matrix. The ferromagnetic particles develop particle-to-particle attraction forces in the presence of a magnetic field, yielding a gross average stiffness increase.

While ferromagnetic inter-particulate attraction causes a stiffness increase in magnetic fields, the presence of any particulate matter in an elastomer contributes additional stiffness to an otherwise unfilled elastomer. An analytical model relates the amount of particulate matter in an elastomer to the overall Young's modulus such that [18]

$$E\prime = E_0(1 + 2.5\phi + 14.1\phi^2), \tag{2.3}$$

where ϕ is the volume fraction of the elastomer composite that consists of the particulate matter, and E_0 is the unfilled elastomer's Young's modulus. This model remains accurate, even when particulate matter is not randomly aligned [18]. Meinecke experimentally validated this model [27].

MREs yield the largest stiffness changes when they have been cured in the presence of a magnetic field [7]; it has become common practice to cure MREs in this manner. When a magnetic field is present during cure, iron particles within the MRE align in chains, as shown in Figure 2.2. This means that the cured MRE exhibits isentropic, or non-directionally uniform, behavior in response to magnetic fields.

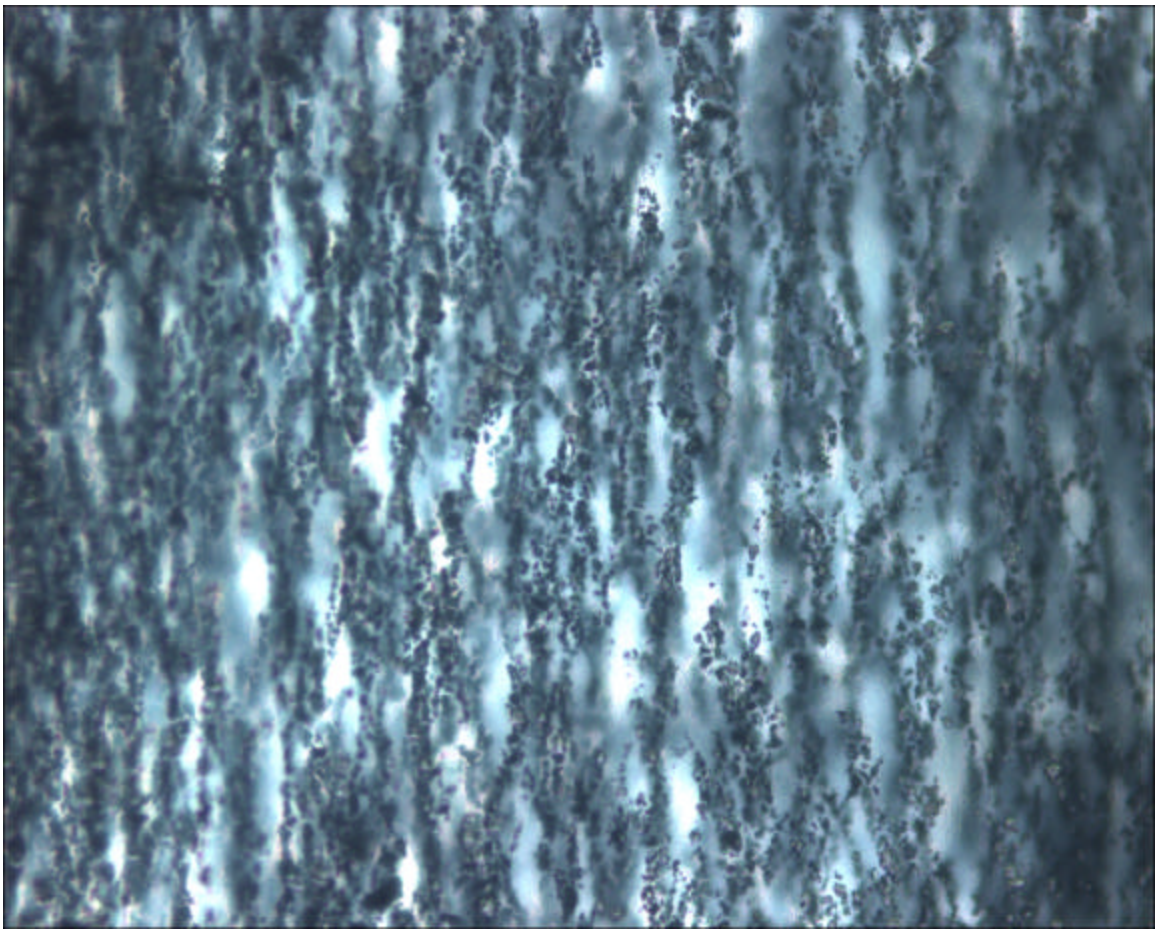

Figure 2.2: An MRE, made up of 30% iron particles by volume, is magnified by a factor of 1000. The iron particles are aligned in chains.

Figure 2.3 depicts an isentropic MRE excited in three different orientations. Each orientation places MREs such that the chains within the MREs are parallel to the direction of magnetic field. However, the shear mode device, on the left, is excited perpendicular to the magnetic field, whereas the longitudinal and squeeze-mode devices, on the center and right, are excited parallel to the direction of the magnetic field. The primary difference between a longitudinal mode and squeeze mode device is that the longitudinal mode device has static separation distance between the base and absorber masses, enforced by geometric conditions and independent from spring stiffness, while the static separation distance for the squeeze-mode absorber is dependent upon the MRE's stiffness.

Research on MREs excited in shear was first conducted by Rigbi and Jilken in 1983 [31],

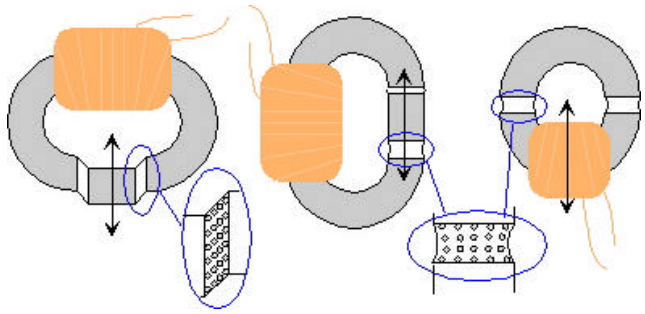

Figure 2.3: MREs placed in shear, longitudinal, and squeeze modes

when a stable magneto-mechanical state was found to exist within MREs. MREs have been developed for variable stiffness suspension applications [38, 17]. MREs containing 27% iron by volume have been found to generate the largest stiffness increase, of up to a 50% stiffness change [10]. This corresponds to approximately a 23% natural frequency increase.

While MREs have been studied extensively when excited perpendicular to the direction of magnetic field [40, 33, 23, 16, 10], little work has concentrated on the mechanistic explanation governing MRE behavior when excited parallel to the direction of magnetic field. Furthermore, the mechanistic explanation for the stiffness increase in shear does not apply to a stiffness increase experienced by an MRE excited in a longitudinal or squeeze mode application.

MREs in the longitudinal and squeeze mode orientations have been studied for magnetostrictive as well as dynamic characteristics. Researchers have investigated the magnetostriction properties of MREs, which includes static geometric changes in MREs due to magnetic fields. Dynamic studies of MREs in longitudinal modes have been explored only recently, with publications dating back to 2002 by Sun et al [36]. While the theoretical rationale for a stiffness increase in this orientation was up to 2008 unknown, Lerner and Cunefare found as much as a 507% natural frequency increase when excited in this manner [26]. This natural frequency increase was significantly larger than the frequency increase exhibited in the shear mode. This large frequency increase can potentially be useful in a variety of control applications such as beam vibration control, where the second vibration mode is roughly 5.27 times larger than the fundamental natural frequency [28]. For cases

such as these, Holdhusen and Cunefare found that beams can be optimally controlled if a spring stiffness could increase by a factor of 1.94 [21].

Magnetostriction has been studied for MREs with iron fraction volumes of at least 27% [5, 42]. One of the interesting magnetostrictive properties exhibited by MREs are its change in nominal length, or static length, in response to the application of a constant magnetic field. MRE static lengths have been found susceptible to MRE filler content and the ratio of void volume within the MRE to overall volume [4]. MRE static length was found to decrease linearly with increasing flux density B, measured in Tesla, or

$$\epsilon = \frac{\Delta l}{l_0} \propto -B \tag{2.4}$$

for $B < 0.3$ T and for ϕ =0.4, 0.6, and 0.8 [5]. Significant hysteretic effects were also found. Magnetostatic volumetric changes were predicted using eigenstrains and Eshelby's equivalent inclusion method [36], which models strain induced by inhomogeneity by replacing particulate matter with the matrix material. Experimental work has found that while MREs cured in the presence of a magnetic field will decrease in length along the direction of a magnetic field, an MRE cured in the absence of a magnetic field, called an elastomer-ferromagnet composite (EFC), will actually increase in length along the axis of a magnetic field as random particles migrate normal to the field in an effort to align into chains [42].

While significant efforts have been placed on examining the theoretical reasoning behind MRE behavior in the static realm, few explanations have been offered for dynamic behavior of MREs in the longitudinal direction. Brigadnov et. al. attempted to explain MRE behavior by developing an isotropic model of MREs [8]. A reasonable match was achieved between the theoretical model and shear data collected from Jolly et al. [22], but this mathematical model has not been compared to longitudinal experimental data.

Zhou and Li have claimed that low-frequency applications of MREs are futile [43]. After studying acceleration hysteresis curves, Zhou and Li concluded that MREs do not exhibit frequency changes in the presence in a magnetic field [43]. They found little change in the acceleration curves when magnetic fields were applied for excitation frequencies below 80 Hz, and inferred that MREs are not useful for low-frequency applications [43]. (It should be

noted that they did not record the natural frequency of the system they studied.) However, this work was looking at the response of MREs to specific frequency excitations; it was a well-known phenomenon that the response of a vibration absorber well below its natural frequency remains constant; the key was to develop an MRE with a low natural frequency to operate in low frequency applications.

Farshad and Benine found experimentally that compressive moduli can increase by a factor of 3 when subjected to a magnetic field [12]. Furthermore, it was found that MREs experience the largest property shifts in the direction of iron particles when iron particles are aligned [26, 12].

2.3 Elastomer modeling

Iron particle alignment within MREs is possible because an elastomeric substrate holds the ferromagnetic particles in place. Elastomeric stiffness behavior has been studied intensely because as a class they exhibit elastic characteristics. This section examines how elastomers deviate from other material models of stiffness moduli, and commonly accepted elastomeric models.

Elastomers, like many materials, deform in a manner best governed by Hooke's Law, where

$$\sigma = E\epsilon, \tag{2.5}$$

and σ is stress, E is the material's Young's modulus, and ϵ is strain. However, elastomers used in MRE applications are generally considered to have complex Young's moduli [15, 41], since the stress and strain are generally out-of-phase with each other. The difference in phase is captured by a loss factor, δ, where

$$\tan(\delta) = \frac{E"}{E'}, \tag{2.6}$$

$E"$ is the viscous out-of-phase Young's modulus and E' is the elastic in-phase Young's modulus. A complex Young's modulus, E^*, creates a phase lag between stress and strain as well as displacement-dependent energy loss.

2.4 Magnetic field models

MREs contain both elastomers, discussed in the previous section, and ferromagnetic particles, discussed here. Ferromagnetic particles are known to undergo a hysterisis loop when in the presence of a magnetic field, as shown in Figure2.4. When a ferromagnetic particle is in the presence of a magnetic field (H), the concentration of the magnetic field, or flux density (B) increases nonlinearly. The ferromagnetic particle is at state (B_x, H_x) at complete saturation. However, once the magnetic field is removed, there will still be some residual magnetic field, or coercive "force", denoted as H_c [19].

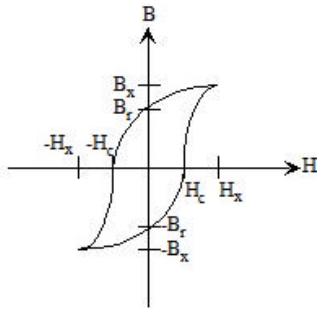

Figure 2.4: A hysteretic loop showing magnetic flux versus magnetic field for a typical ferromagnetic particle.

A standing body of knowledge exists concerning MREs operating in shear, as well as magnetic modeling for ferromagnetic, para- and dia-magnetic materials operating under repulsive magnetism. While this knowledge does not directly address MRE behavior in the longitudinal mode, some of this information can be adapted to describe its performance. This section describes magnetic models for each of these scenarios.

One reason that MREs have been studied extensively in shear as opposed to longitudinal mode may be that there was a theoretical explanation for a stiffness increase in the shear direction. Ferromagnetic particulate matter in MREs are modeled as point dipoles, depicted in Figure 2.5, where the interaction energy between two magnetic dipoles is modeled as

$$E_{ij} = \frac{1}{4\pi\mu_{rel}\mu_0}\left[\frac{\overrightarrow{m}_i \cdot \overrightarrow{m}_j - 3\left(\overrightarrow{m}_i \cdot \widehat{e}_r\right)\left(\overrightarrow{m}_j \cdot \widehat{e}_r\right)}{\left|\overrightarrow{r}\right|^3}\right], \tag{2.7}$$

where μ_{rel} is the relative magnetic permeability, $\mu_0 = 4\pi \times 10^{-7}$ is the magnetic permeability

of a vacuum, $\overrightarrow{m}_i$ and $\overrightarrow{m}_j$ are magnetic strengths of each magnetic particle, assumed to be identical and saturated in high magnetic fields, and $\overrightarrow{r}$ is the distance of separation between particles i and j. When excited in shear, the total energy per unit volume is [23]

$$U = \frac{3\phi\left(\epsilon^2 - 2\right)\left|\overrightarrow{m}\right|^2}{2\pi^2\mu_{rel}\mu_0 d^3 r_0^3\left(1+\epsilon^2\right)^{7/2}}, \tag{2.8}$$

where ϕ is the fraction of particulate matter, by volume, ϵ is the strain in shear, defined as $\epsilon = x/r$. The shear stress is then defined as

$$\sigma = \frac{\partial U}{\partial \epsilon} = \frac{9\phi\epsilon\left(4 - \epsilon^2\right)\left|\overrightarrow{m}\right|^2}{2\pi^2\mu_{rel}\mu_0 d^3 r_0^3\left(1+\epsilon^2\right)^{7/2}}, \tag{2.9}$$

where d is the diameter of the particles. If small strain are assumed, or $\epsilon < 0.1$, the shear modulus is

$$G \simeq \frac{\phi J_p^2}{2\mu_{rel}\mu_0 h^3}, \tag{2.10}$$

where h is the height of the MRE, and J_p is the saturation polarization of the particles with an MRE, and $J_p \propto H$. This means that $\Delta G \propto H^2$, where H was the applied magnetic field intensity, for dipole-dipole interactions [33]. Davis empirically confirmed this relationship in 1999 [10]. Davis also found a relationship that described maximum possible change in shear modulus [10] such that

$$\frac{\Delta G_{\max}}{G\left(0\right)} = \frac{0.1911\text{MPa}}{G_0}, \tag{2.11}$$

and for a "typical" elastomer with $G_0 = 0.4$ MPa, he predicted a 50% increase for the optimal particle volume fraction. However, Lerner and Cunefare found that larger increases can be achieved with elastomers containing much softer shear moduli. Using a shear modulus of 250 Pa, they found a 335% increase in modulus.

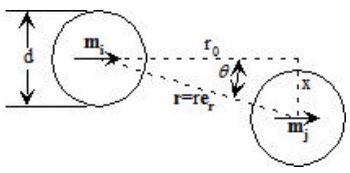

Figure 2.5: Two magnetic particles.

Ferromagnetic particles can only be modeled as magnetic dipoles when they are in high magnetic fields. Ginder found a sub-square relationship between G and H for nonsaturated iron particles [14]. Zhou stated further that the magnetic dipole assumption does not hold true for magnetic fields lower than 0.8 Tesla, and that local magnetic saturation in particles must be included for these cases [40]. Ginder et al [16] predicted analytically that for intermediate fields, $u = -\frac{3}{8}\phi\mu_0 M_s^2 \left(\frac{\delta}{R}\right)^4$, where M_s is the magnetic saturation, δ is the radius of the saturation zone, and R is the radius of the particle. Jolly et al. examined MREs and MR fluids when particles are partially saturated, as would be the case for intermediate fields, and found theoretical curves that fit MR behavior [22]. Shkel and Klingenberg modeled an MR chain assuming point-dipole model, but modeled the relative magnetic permeability according to the Frolich-Kennelly equation, such that [34]

$$\mu_{rel}(H) = 1 + \frac{(\mu_0 - 1)M_s}{(\mu_0 - 1)H + M_s}. \tag{2.12}$$

The Frohlich-Kennelly model describes magnetic permeability very well for intermediate and large magnetic fields, but does not reflect low magnetic field behavior well. This type of modeling remains suitable for shear excitation in intermediate and large magnetic fields.

MREs have not been modeled extensively in squeeze and longitudinal modes. Since their mechanistic behavior was not well understood, a search was conducted to investigate other implementations of magnetic fields in attraction or repulsion. It was possible that these types of magnetic field models could lead to an explanation of squeeze and longitudinal MRE behavior.

Magnetic fields are used in magnetic bearing, levitation, and repulsion systems. These three systems are effectively one phenomenon; that is, magnetic levitation, or maglev, systems feature two magnets, operated in repulsion. The force of the repulsion allows a mass attached to the nonstationary magnet to be suspended, reducing the effects of friction. Figure 2.6 shows a typical magnetic levitation system. One magnet, typically one with variable and controllable magnetic field output, is fixed to a system, and the second magnet, which is a permanent magnet, is then suspended.

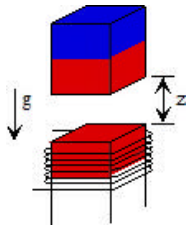

Figure 2.6: A magnetic levitation system works by applying a magnetic force that opposes gravity.

The maglev phenomenon was investigated by conducting a numerical study of two permanent magnets, separated by an air gap, z. The repulsive magnetic force was found to follow $F_z = k/z$, where k is a constant [37]. It was found that a linearized magnetic force could be integrated into an equation of motion such that

$$m\ddot{\varsigma} + c\dot{\varsigma} + mg - \left(\frac{k}{z_0}\right) + \left(\frac{k}{z_0^2}\right)\varsigma - \left(\frac{2k}{z_0^3}\right)\varsigma^2 = F(t), \tag{2.13}$$

where $z = z_0 + \varsigma$, and $F(t)$ is a control force [37]. The second-order magnetic forcing effect can generally be discarded. The remaining two terms generate two effects; the 0^{th}-order effect decreases the net static displacement of the suspended magnet, and the 1^{st}-order effect generates a net stiffness between the two magnets. While repulsive maglev systems are stable in the axial direction, any transverse displacement will generate instability. However, two-axis repulsive control systems can be created to generate a stable control system [39].

Repulsive magnetism can also be used to alter mechanical behavior of para- and dia-magnetic materials, such as aluminum, copper, or brass. Consider Figure 2.7, where a para- or dia-magnetic material is positioned as a vibrating cantilever beam, in between two permanent magnets of identical strength. The Joule effect generates induced current through the cantilever beam. This induces a "phantom effect", which is modeled as a force proportional to the velocity of the beam, such that [30]

$$F_m = \alpha\left(\frac{\partial B}{\partial x}\right)^2 \dot{x}, \tag{2.14}$$

where α is a constant, and $\partial B/\partial x$ is the flux density gradient as a function of x. In this way, permanent magnets can be used to increase the viscous damping in a system if the system to be controlled was a para- or dia-magnetic material.

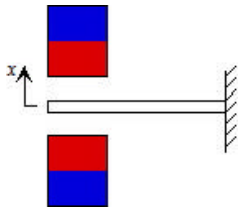

Figure 2.7: A paramagnetic material in between two permanent magnets in repulsion.

There has been significant work conducted on MREs in shear, magnetic modeling for repulsive control systems both in ferro-magnetic as well as para- and dia-magnetic materials, and magnetostriction modeling conducted on MREs in the longitudinal direction.

Chapters V, VI, and VII describes MRE behavior when the MREs are excited in a longitudinal manner. In Chapter III, elastomeric and magnetic models discussed in this chapter are used to model microscopic pieces of MREs as matrices of elastomer and iron particles.

CHAPTER III

NUMERICAL MODEL

A numerical model was developed to answer the questions: "how do loss factors and natural frequencies vary with magnetic field?" and "what is the characteristic response time of MREs subjected to a step change in magnetic field?". In order to address these questions, a simulation is constructed by combining basic magnetic theory with linear vibration theory. The simulation results are validated against experimental data in Chapter VI. The contents of this chapter develop the underlying principles behind the simulation and validate the curve-fitting method used to answer the dissertation questions.

The work presented in this chapter addresses the general numerical model used to determine a small MRE's dependency on magnetic field at a microscopic scale. Each micro scale model is used as a basic building block and stacked upon itself to create larger MRE assemblies. The change in key characteristic behavior was identified and used to numerically extrapolate macro scale MRE behavior. Section 3.1 discusses the characteristic elastomer and iron properties used and assumed for this dissertation work, which are applied in the remainder of this work. Section 3.6 describes scaling techniques used to validate this micro-scale numerical model using macro-scale elastomeric results.

3.1 Modeling MREs: Representative Characteristics

In this work, MRE behavior was measured experimentally, simulated numerically, and their results were compared. In order to make like comparisons, simulation properties mirrored the experimental properties. This section lists the material and behavioral properties that were used in this work to assess MRE behavior.

While many MRE applications contain base elastomers with shear moduli of approximately 0.4 MPa [33], this research follows a continuation of prior work aimed at developing a low-mass, low-frequency SSA [2]. A base elastomer, discussed more thoroughly in Chapter

IV, was represented in the numerical models as having a Young's modulus of $E = 1.3$ MPa, a characteristic mass of 66 picograms, and a loss factor of 0.2. These two properties were found experimentally to best represent this elastomer [25]. The ferromagnetic particles in this work were iron microparticles. They were modeled as spheres with an average diameter of 7 μm, and a characteristic mass of 0.36 ng.

The magnetic field inside the elastomer was modeled such that a saturation magnetic flux of $B_m = 1.4$ T required a separation force of

$$F_m = \frac{B_m^2}{2\mu_0\mu_{rel}}, \tag{3.1}$$

where μ_{rel} was assumed to be 1, since pure elastomers have ferromagnetic properties similar to air.

3.2 Numerical models for MREs

MREs are commonly modeled as springs placed between a base mass and an absorber mass, simulating conditions depicted in Figure 2.1. The equations discussed in Sections 3.2.1.1 and 3.2.1.2 are compiled into a model that simulated MRE performance in such a configuration.

When MREs are modeled, typically the global material properties are applied to an FEA program. This means that for each different MRE used, the MREs must first be tested to identify material properties before further FEA analysis can be conducted. The purpose of generating the models discussed in this chapter and for the duration of this dissertation is to create a model that addresses the microscopic behavior in terms of base elastomer characteristics as well as particle properties and to predict macroscopic trends. The advantage to this type of model is that elastomer and particle properties are generally well-known, and MREs need not be created in order to do initial testing.

In order to model MRE behavior, microscopic cross sections of MREs were modeled as matrices of connected elements. Appendix A lists the ensemble of all MRE matrices that were used in this work. MRE behavior is first modeled in the absence of a magnetic field, and then modified to include the particles linked in chains by a magnetic field. The modeling details are presented in Section 3.2.1.

3.2.1 MRE models and equations of motion (EoMs)

MREs contain chains of particles that move together as a single unit in high magnetic fields under low forcing conditions, but move independently under large forcing levels or low/nonexistent magnetic fields. The elastomer elements, on the other hand, are modeled as mass and spring elements in all cases. The system of equations are established for an MRE assuming no external magnetic field in Section 3.2.1.1, and the effects of the magnetic field are addressed in Section 3.2.1.2.

3.2.1.1 MRE system of equations with no magnetic field

Figure 3.1 shows a sample MRE matrix Actual matrices used for this work can be found in Appendix A. MREs were modeled as matrices of elements, where each element is assigned a value of either spring or magnetic particle, and each element's motion is described by an equation of motion. Element locations were predicted for each step in the following order:

1) Forcing elements – all elements along the bottom rows
2) Unbroken long-chain particle elements (only in magnetic fields)
3) All other particle elements – denoted by the crosshairs in Figure 3.1

The equations of motion for each particle element were compiled so that the displacement of all particles could be predicted at time step $i+1$ using a linear time invariant (LTI) model such that

$$\begin{Bmatrix} \dot{x}_{i+1} \\ \ddot{x}_{i+1} \end{Bmatrix} = \begin{Bmatrix} [0] & [I] \\ [M]^{-1}[A] & [M]^{-1}[B] \end{Bmatrix} \begin{Bmatrix} x_i \\ \dot{x}_i \end{Bmatrix} + \begin{Bmatrix} 0 \\ [M]^{-1} F_{i+1} \end{Bmatrix} \tag{3.2}$$

and

$$\begin{Bmatrix} x_{i+1} \\ \dot{x}_{i+1} \end{Bmatrix} = \begin{Bmatrix} \dot{x}_{i+1} \\ \ddot{x}_{i+1} \end{Bmatrix} \cdot dt + \begin{Bmatrix} x_i \\ \dot{x}_i \end{Bmatrix}, \tag{3.3}$$

where $[I]$ is an identity matrix, $[A]$, $[B]$ and $[M]$ are matrices determined through the EoM, F is a forcing vector, and dt is the time between each time step.

In order to determine matrices $[A]$, $[B]$, and $[M]$, each element is classified as either an elastomer or a particle. The elastomer in this cross section is represented as longitudinal springs, with spring constants equal to the stiffness of an equivalently sized elastomer and

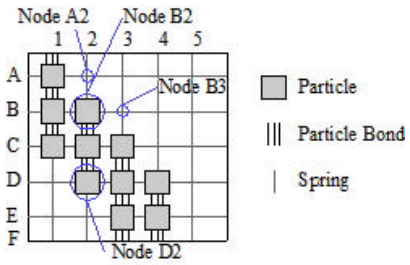

Figure 3.1: Schematic representation of a microscopic cross section of a sample MRE. Letters and numbers designate the element grid.

containing a point mass at the node location of an equivalent size. The particles were represented by point masses of iron. Shear springs, whose stiffnesses were equivalent to the host elastomer's, connected neighboring elements in the direction perpendicular to that of the excitation. All elements along the bottom of the sample moved together uniformly according to the forcing displacement, and the top of the sample is fixed at a zero reference frame.

Each element's behavior is characterized by an equation of motion, described as

$$(1-\beta_{mn})\,M\ddot{x}_{mn} = -\sum_i \sum_j \left[\alpha_{ij}k_{ij}\left(x_{mn}-x_{ij}\right)+\alpha_{ij}c_{ij}\left(\dot{x}_{mn}-\dot{x}_{ij}\right)\right]+\beta_{mn}f, \tag{3.4}$$

where α_{ij} is 1 if element ij is immediately adjacent to element mn, otherwise it is 0, and the summation indicates all elements directly adjacent to element(m,n). β_{mn} is an indicator; if element(m,n) is in the bottom row, β_{mn} is 1, otherwise it is 0. M is the mass at element(m,n). The stiffness k_{ij} is either a longitudinal or shear stiffness, depending on whether element(i,j) is adjacent to, or above/below element(m,n). The variable f is the forcing function applied to the bottom row of the MRE matrix.

Equation 3.4 is implemented for every particle in each MRE. Consider a sample MRE, depicted in Figure 3.1. The equation of motion for element A2 would be

$$\begin{aligned} m_k\ddot{x}_{A2} = &-k\left(x_{A2}-0\right)-k\left(x_{A2}-x_{B2}\right)-k_s\left(x_{A2}-x_{A1}\right)-k_s\left(x_{A2}-x_{A3}\right) \\ &-c\left(\dot{x}_{A2}-0\right)-c\left(\dot{x}_{A2}-\dot{x}_{B2}\right)-c_s\left(\dot{x}_{A2}-\dot{x}_{A1}\right)-c_s\left(\dot{x}_{A2}-\dot{x}_{A3}\right), \end{aligned} \tag{3.5}$$

where k and c are the tensile stiffness and damping, respectively, m_k is the mass of the spring element, and k_s and c_s are the shear stiffness and damping. The equation of motion

for element B2 would be

$$m\ddot{x}_{B2} = -k(x_{B2} - x_{A2}) - k_s(x_{B2} - x_{B1}) - k_s(x_{B2} - x_{B3}) - \tag{3.6}$$
$$c(\dot{x}_{B2} - \dot{x}_{A2}) - c_s(\dot{x}_{B2} - \dot{x}_{B1}) - c_s(\dot{x}_{B2} - \dot{x}_{B3}),$$

where m is the mass of the particle. Since element C2 is also a particle, it does not contribute to B2's motion in the absence of a magnetic field. Equation 3.4 describes the motion of every element except for those in the bottom row. elements in row F are dictated by the forced motion f, such that

$$x_{F_j} = f, \tag{3.7}$$

where $j = \{1, 2, 3, 4, 5\}$. Equations 3.5, 3.6, and 3.7 can be rearranged into the general matrix equation of

$$[M]\ddot{x} + [B]\dot{x} + [A]x = \overrightarrow{F}. \tag{3.8}$$

One important characteristic of the mass matrix $[M]$ is that it is a diagonal matrix, where the diagonal is the mass of each particle. This value is zero when an element is positioned along the bottom row of the MRE, such as described by Equation 3.7. Therefore, the mass matrix is singular, and Equation 3.8 cannot be applied to Equation 3.2.

A modified mass matrix must be constructed in order to correctly produce Equation 3.2. All bottom row elements can be given a nominal diagonal matrix value of 1, and once $[M]^{-1}$ has been calculated, the resultant diagonal is replaced with 0. This means that Equation 3.3 must be modified to ensure that bottom element motion is being properly calculated. The $(i+1)^{th}$ time step is calculated such that

$$x_{i+1} = Ax_i + F. \tag{3.9}$$

Equations 3.2 and 3.3 are used to describe an MRE's dynamic performance in the absence of a magnetic field. These equations are the bases for determining the behavior of MREs in a magnetic field. The EoM for MREs in a magnetic field are described in Section 3.2.1.2.

3.2.1.2 MRE system of equations in a magnetic field

When neighboring iron particles are in the presence of a magnetic field that dominates other forcing effects, these iron particles move as a unit. As other forcing factors increase and become stronger than the magnetic field, the iron particle unit break into smaller units, and then finally as individual particles. This section describes the models used to predict this behavior.

Full Chain EoMs Consider the chain of particles in Figure 3.1 comprised of elements B2, C2, and D2. Using the methods described in Section 3.2.1.1, the EoMs for these elements are

$$\begin{aligned}
B2: &\quad m\ddot{x}_{B2} + (k+2k_s)x_{B2} - k_s(x_{B1}+x_{B3}) - kx_{A2} + (c+2c_s)\dot{x}_{B2} - \\
&\qquad c_s(\dot{x}_{B1}+\dot{x}_{B3}) - c\dot{x}_{A2} = 0 \\
C2: &\quad m\ddot{x}_{C2} + 2k_s x_{C2} - k_s(x_{C1}+x_{C3}) + 2c_s\dot{x}_{C2} - c_s(\dot{x}_{C1}+\dot{x}_{C3}) = 0 \quad . \\
D2: &\quad m\ddot{x}_{D2} + (k+2k_s)x_{D2} - k_s(x_{D1}+x_{D3}) - kx_{E2} + \\
&\qquad (c+2c_s)\dot{x}_{D2} - c_s(\dot{x}_{D1}+\dot{x}_{D3}) - c\dot{x}_{E2} = 0
\end{aligned} \tag{3.10}$$

These three particles will move as a unit because the magnetic attractive forces that bring these particles together exceed the external mechanical forces. Since these three particles are moving as a unit, $\ddot{x}_{B2} = \ddot{x}_{C2} = \ddot{x}_{D2}$. Exploiting Newton's 2^{nd} Law, the chain's equation of motion can be written as

$$\begin{aligned}
3m\ddot{x}_{D2} + (k+2k_s)(x_{B2}+x_{D2}) + 2k_s x_{C2} - k_s(x_{B1}+x_{B3}+x_{C1}+x_{C3}+x_{D1}+x_{D3}) - \\
k(x_{A1}+x_{B2}) + (c+2c_s)(x_{B2}+x_{D2}) + 2c_s x_{C2} - \\
c_s(x_{B1}+x_{B3}+x_{C1}+x_{C3}+x_{D1}+x_{D3}) - c(x_{A1}+x_{B2}) = 0
\end{aligned} \tag{3.11}$$

This equation of motion can be used to describe element D2's motion. Elements C2 and B2 can then be rewritten such that

$$\begin{aligned}
x_{C2} &= x_{D2} - \delta x \\
x_{B2} &= x_{C2} - \delta x
\end{aligned} , \tag{3.12}$$

where δx is the distance between the center of the particles, or the diameter of the particle, if they are spherical. These findings can be generalized for a chain of N particles, such that

$$\begin{aligned} x_j &= x_{j+1} - \delta x && \text{for} \quad j = 1, 2, \ldots, N-1 \\ Nm\ddot{x}_N &= -(\sum_{j=1}^{N} \overrightarrow{K}_j) \cdot \overrightarrow{x} - (\sum_{j=1}^{N} \overrightarrow{C}_j) \cdot \overrightarrow{\dot{x}} && \text{for} \quad j = N \end{aligned} \tag{3.13}$$

where $\overrightarrow{K}_j$ is the j^{th} row of the stiffness matrix and $\overrightarrow{C}_j$ is the j^{th} row of the damping matrix. Equation 3.13 is incorporated into Equation 3.3 for large chains.

Chain Breaks In section 3.2.1.2, EoMs were derived for an MRE in a large magnetic field but subjected to a small excitation force. In section 3.2.1.1, EoMs were derived for an MRE under no magnetic field, but this derivation also holds for an MRE in a magnetic field with large excitation. While these EoMs capture MRE behavior at the extremes of expected excitation behavior, there is a range of intermediate stages between these two extremes for which these models are not representative. In physical terms, these intermediate stages represent the different interactive forces when the magnetic chains inside an MRE are breaking and there are any number of smaller chains and some independent particle motion. The derivation of these intermediate stage EoMs is detailed in this subsection.

Intermediate stage EoMs are calculated in an iterative manner, and are dependent upon the internal structure of the MRE. When MREs contain long chains, defined as chains that connect the top and bottom of the MRE, the long chains must be broken first. Beginning with the EoMs derived in section 3.2.1.2, the location of the first chain break must be determined, and then the EoM of the MRE with this newly broken chain may be determined. For each subsequent stage, the order of particle bond breaks must first be found, and then the EoM may be derived.

In order to determine where a chain break occurs within a specific chain, consider the chain comprised of elements B2, C2, and D2 in Figure 3.1. Immediately prior to the first chain break, the MRE will be operating under conditions established by the EoMs in Equation 3.13. If the excitation force subjects the MRE to a step increase in displacement

of dx, the MRE's new static equilibrium can be found by solving

$$[K]\vec{x} = \vec{F}, \tag{3.14}$$

where $[K]$ is the stiffness matrix as established by Equations 3.4, 3.3, and 3.13, assuming that $\ddot{x}_{ij} = 0$ for all i and j.

As an MRE is stretched, forces on each particle chain increase until the forces due to the excitation overcome the attractive magnetic forces. Although each particle within a chain moves uniformly, and generally adheres to rigid body mechanics, this holds true only while the forces internal to the chain are less than the force required to separate two magnetic particles,

$$F_m = \frac{B^2 A}{2\mu_{rel}\mu_0}, \tag{3.15}$$

where B is the magnetic flux, in Tesla, A is the common surface area that the two particles share when in contact, μ_{rel} is the relative permeability, where $\mu_{rel} = 200$ for iron, and μ_o is the magnetic permeability in a vacuum, or $\mu_0 = 4\pi \times 10^{-7}$. Since each particle is individually attached to different springs, the particle that builds up enough separation force from its neighbors will break off first. Once that chain break has occurred, assuming a uniform particle size and contact area, the attractive magnetic force between two particles in a constant magnetic field is a constant value. In a static balance situation, the step displacement due to a chain separation is found to be

$$dx = \frac{B^2 A}{2k\mu_{rel}\mu_0}. \tag{3.16}$$

The net magnetic force in this work is modelled as

$$F_i = \left\{ \begin{array}{l} m_i\left(\ddot{x}_i - \ddot{x}_{i-1}\right) \text{ if } m_i\left(\ddot{x}_i - \ddot{x}_{i-1}\right) < F_m \\ F_m \text{ if } m_i\left(\ddot{x}_i - \ddot{x}_{i-1}\right) \geq F_m \end{array} \right\}, \tag{3.17}$$

where F_i is the attractive magnetic force between the i^{th} and the $(i-1)^{th}$ element. The magnetic force forces the ith and $(i-1)^{th}$ elements to move together if the force separating them is less than the threshold magnetic force described in Equation 3.15. However, the attractive magnetic force is assumed to be a constant value for any separation forces greater

than that. By modeling magnetic forces in this way, the nonlinear decrease in magnetic field is ignored. This technique is valid for small displacement values; in the future, the effect of such an assumption may be studied in greater detail.

3.2.2 Comprehensive, micro scale MRE models

Whereas section 3.2.1 describes elastomer motion and section 3.2.1.2 discusses the motion of particles in chains, this section synthesizes the analyses developed in the previous two sections, and describes a system of equations that predict MRE constituent behavior for a microscopic building block like that depicted in Figure 3.1. Equations 3.2 and 3.3 give a framework for finding the next time step in an MRE simulation. Within this framework, particle motion is calculated within each iterative step before elastomer motion. Since particles are assumed to have mass, they are treated as point masses within the MRE, whereas elastomer elements are assumed to be point springs, massless, and therefore in static equilibrium at all times (the lack of a static condition notwithstanding).

For this analysis, the entire vector of the elastomer's nodes can be regrouped so that at time j the position vector is

$$x_j = \left\{ \begin{array}{c} x_{part,j} \\ \\ x_{forcing,j} \end{array} \right\}, \tag{3.18}$$

where $x_{part,j}$ is a vector containing all the particles' displacement. The vector $x_{forcing,j}$ describes all the elements in direct contact with the forcing element, and overrides those elements' dynamic behavior as particles. If there are p elements in x_{partj} and f elements in $x_{forcingj}$, then $n = p + f$. From Equation 3.9, A can be rewritten such that

$$Ax = \left(\begin{array}{cc} [A_{pp}] & [A_{pf}] \end{array} \right) \left\{ \begin{array}{c} x_{part,j} \\ \\ x_{forcing,j} \end{array} \right\}, \tag{3.19}$$

where A_{pp} is $p \times p$ and A_{pf} is $p \times f$.

Particle motion is derived from the general iterative form where

$$\begin{aligned} \dot{x} &= Ax + B \\ y &= Cx + D \end{aligned} \tag{3.20}$$

for a continuous system, and $\dot{x}$ is found from Equation 3.9. Since the outcome of this method is a numerical simulation, this equation must be discretized, so that

$$x_{i+1} = Ax_i + B. \tag{3.21}$$

These equations are tailored to the MRE simulation such that the motion of a vector of all particles within an MRE can be calculated by

$$x_{part,j} = e^{A_{pp}dt} + A_{pp}\left(e^{A_{pp}dt} - I\right)\left(A_{pf}x_{forcing,j}\right), \tag{3.22}$$

where A_{pp}, and A_{pf} are described in Equation 3.19.

Two matrices must be defined in order to use Equations 3.22 and 3.2. In order to find A_{pp} and A_{pf}, recall from Equation 3.4 that the equation of motion for a particle in a continuous system is

$$m_{mn}\ddot{x}_{mn} = -\sum_i \sum_j \left\{\alpha_{ij}\left[k_{ij}\left(x_{mn} - x_{ij}\right) + c_{ij}\left(\dot{x}_{mn} - \dot{x}_{ij}\right)\right]\right\}, \tag{3.23}$$

where α_{ij} is 1 if x_{ij} is a neighboring element to x_{mn}, and 0 otherwise. The mass element, $m_{mn} = N\left(\Delta m\right)$, is the mass of each elemental particle, Δm, multiplied by the number of particles in the chain, N. Equation 3.23 can be rearranged such that

$$\ddot{x}_{part} = A_{pp}x_{part} + A_{pf}x_{forcing} + B_{pp}\dot{x}_{part} + B_{pf}\dot{x}_{forcing}. \tag{3.24}$$

Equation 3.23 and its discrete counterpart, Equation 3.22, hold only for the last element of a chain that does not terminate on the forcing surface. The rest of the particles in the chain are described by $x_j = x_{j+1} - dx$. It should be noted that for Equation 3.23, $x_{forcing}$ describes the displacement of all elements in contact with the forcing surface, or any element in the M^{th} row.

In summary, a simulation was created using an iterative time-step simulation such that $x_{i+1} = e^{[A]dt}\vec{p} + A\vec{x}_i + \vec{B}$, where

$$A = \begin{bmatrix} [A_{pp}] & [A_{pf}] \end{bmatrix}, \tag{3.25}$$

and

$$x_i = \begin{Bmatrix} x_{part,i} \\ x_{forcing,i} \end{Bmatrix}. \tag{3.26}$$

Each value of A is first identified using equations of motion such that $A_{m,n} = \sum_i \sum_j \alpha_{ij} k_{ij}$ and α_{ij} is 1 if x_{ij} is a neighboring element to x_{mn}, and 0 otherwise. Then A is broken into submatrices A_{pp}, and A_{pf}, according to whether x_{mn} is on the line of forcing or not, and whether its neighboring node is a particle, or forcing unit.

3.3 Using a numerical model to predict MRE behavior

The numerical models, developed in the previous section, are applied to predict experimental MRE behavior. The equations that were discussed in the previous section are used to model the displacement of each node within an MRE at every instance in time. However, only the motion at the ends of the MRE is important in macro scale MREs; this is the motion that is associated with the forcing frequency, and the displacement that is attached to the absorber mass. So while each node is independently modeled for every MRE configuration, the only simulation results used are the time progression, the forcing excitation, and the uniform displacement of the top nodes that would attach to a mass in SSA applications.

The numerical model yields time data, from which properties such as natural frequency and loss factors must be identified. Section 3.4 discusses how single degree-of-freedom absorber models are applied to these simulation results, and how key properties are identified.

3.4 Post-processing: System identification

MRE behavior is simulated according to the methods detailed in Section 3.2. The resultant absorber mass behavior is fit to an equivalent single degree-of-freedom spring-damper vibration model such that

$$\ddot{x}_{abs} + i2\zeta\omega_n\dot{x}_{abs} + \omega_n^2 e^{i\delta} x_{abs} = i2\zeta\omega_n\dot{x}_{base} + \omega_n^2 x_{base}. \tag{3.27}$$

This model is used because the goal is to create a tunable vibration absorber, in particular a tunable vibration absorber whose stiffness is controllably variable. By fitting the simulation results to this curve, natural frequency and damping characteristics can be identified for future control algorithms.

Equation 3.27 was used to identify system properties for all simulations in this work. When discussing natural frequencies, the time response was converted to the frequency

domain via FFT to evaluate frequency response. Figure 3.2 shows a representative frequency response of a 30% MRE (MRE30b) that was excited with no magnetic field. The frequency data fits well to the assumed model described in Equation 3.27. Model identification strategies are compared to find the best fit according to sum of the square of errors.

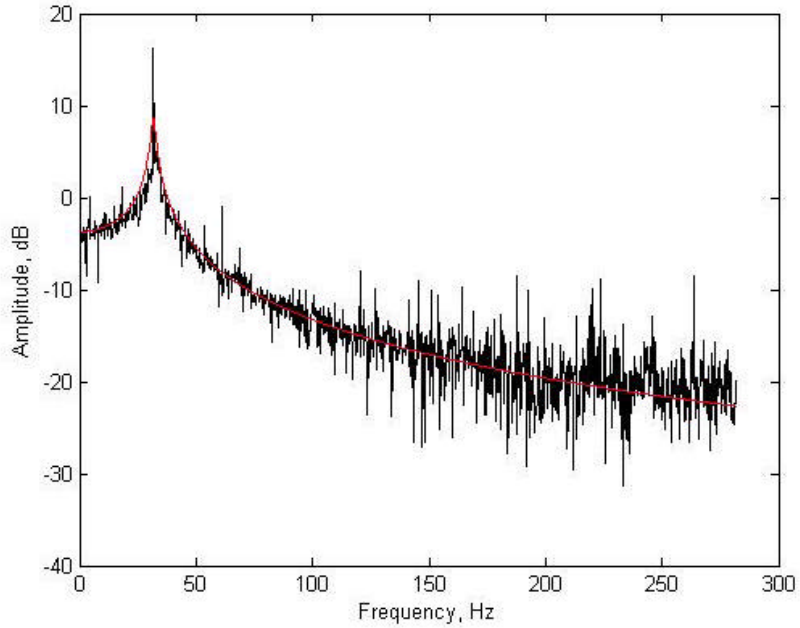

Figure 3.2: The transfer function as a function of frequency for a 30% MRE subjected to a 0.1 forcing ratio, band limited to below 250 Hz, and no static displacement.

When simulation data is fit to the model described in Equation 3.27, x_{base} and x_{abs} were the input and output of the models described in Equations 3.27. The two unknown variables in Equation 3.27 were ζ and ω_n. Nonlinear least squared error methods were used to calculate these properties, as discussed in Section 3.5.

MRE characteristics were identified by fitting the experimental data to a predetermined single degree of freedom vibration absorption model. Experimental data was fit using least-squared error methods. In order to fit the data to a least-squared error method, a purely real stiffness (K) and damping (C) is assumed for an elastomer modeled in Figure

3.3a. The equation of motion for the absorber mass of the device can be expressed as

$$M\ddot{x} + C\dot{x} + Kx = C\dot{y} + Ky, \tag{3.28}$$

where M is the mass of the absorber, x is the displacement of the absorber mass, and y is the displacement of the base mass. If the natural frequency is defined as $\omega_n = \sqrt{K/M}$and the frequency ratio as $r = \frac{\omega}{\omega_n}$, where ω is the frequency of interest, then the Fourier transform of Equation 3.28 can be found, and the amplitude of the SSA with respect to the base mass, is

$$G = \left|\frac{X}{Y}\right| = 10\log_{10}\left(a\sqrt{\frac{1-4\zeta^2r^2}{\left(1-r^2\right)^2+4\zeta^2r^2}}\right)$$
$$= A \;+\; 5\log_{10}\left(1-4\zeta^2r^2\right) - \;5\log_{10}\left(\left(1-r^2\right)^2+4\zeta^2r^2\right), \tag{3.29}$$

where $A = 10\log_{10} a$. This transfer function is similar to, but not identical to the commonly derived transfer function

$$G = \left|\frac{X}{Y}\right| = 10\log_{10}\left(\frac{(F/K)}{\sqrt{\left(1-r^2\right)^2+4\zeta^2r^2}}\right) =$$
$$10\log_{10}(F/K) - 5\log_{10}\left(\left(1-r^2\right)^2+4\zeta^2r^2\right), \tag{3.30}$$

which is generated when a traditional single-degree-of-freedom system is considered, as shown in Figure 3.3b. The transfer functions described in Equations 3.29 and 3.30 (assuming $F/K = 1$) are plotted in dB against r in Figure 3.4. While these two systems are similar, they are not identical. The discrepancies between these two systems are significant enough such that traditional, linear methods to identify system (b) are not valid for system (a). As a result, nonlinear least-squared error system identification techniques were used.

3.5 Gauss-Newton Least-Squares Algorithm

Since the system shown in Figure 3.3a cannot be described by a linear system, a Gauss-Newton least-squares error methodology was used to identify system parameters ω_n, ζ, and A, as they appear in Equation 3.29. In this section, the Gauss-Newton algorithm is described within the context of application to Equation 3.29.

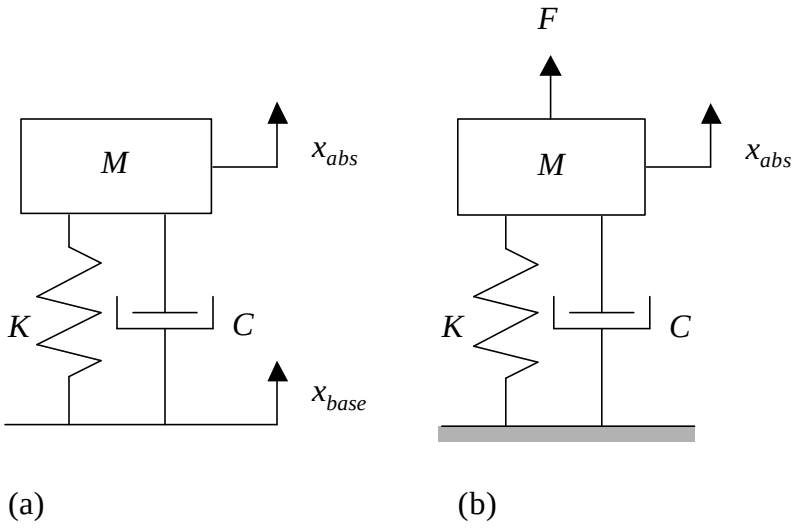

Figure 3.3: Macro-scale representations for a) the system as described in this text, and b) conventionally used to describe single-degree-of-freedom systems.

Figure 3.5 plots numerical simulation data against frequency for a 30% MRE and a curve described by the parameters $A = -0.201$, $\omega_n = 15.3$ Hz, and $\zeta = 0.377$. The parameters ω_n, ζ, and A were found such that $G(\omega_n, \zeta, A)$ best represented the numerically-simulated n-point data (henceforth referred to simply as data) $y(r)$. A 3×1 vector of system parameters was defined as $\beta = [\omega_n, \zeta, A]$, and the Jacobian of the system was a $n \times 3$ matrix such that

$$\mathrm{J}\left(r, \omega_n, \zeta, A\right) = \left[\frac{\partial G}{\partial \omega_n}, \frac{\partial G}{\partial \zeta}, \frac{\partial G}{\partial A}\right]. \tag{3.31}$$

For a transfer function described in Equation 3.29, Equation 3.31 becomes

$$\mathrm{J}\left(r, \omega_n, \zeta, A\right) = \left[\frac{20r^2}{\omega_n \log 10}\left(\frac{2\zeta^2 - 1 + r^2}{den} - \frac{2\zeta^2}{num}\right), \frac{40\zeta r^2}{\log 10}\left(\frac{1}{den} - \frac{1}{num}\right), 1\right], \tag{3.32}$$

where $num = 1 + 4\zeta^2 r^2$ and $den = \left(1 - r^2\right)^2 + (2\zeta r)^2$. The Gauss-Newton algorithm is iterative, and hence dependent upon an initial guess. Given an initial guess $\beta_0 = [\omega_{peak}, 0.2, 0]$, which corresponds to the peak natural frequency, the damping coefficient of the unfilled elastomer, and no amplitude offset, any i^{th} iteration can yield system parameters such that $\beta_i = \beta_{i-1} + \delta\beta$, where

$$\delta\beta = \left[\mathrm{J}^{\mathrm{T}}\mathrm{J}\right]^{-1} \mathrm{J}^{\mathrm{T}}\left[y\left(r\right) - G\left(r, \beta_{i-1}\right)\right]. \tag{3.33}$$

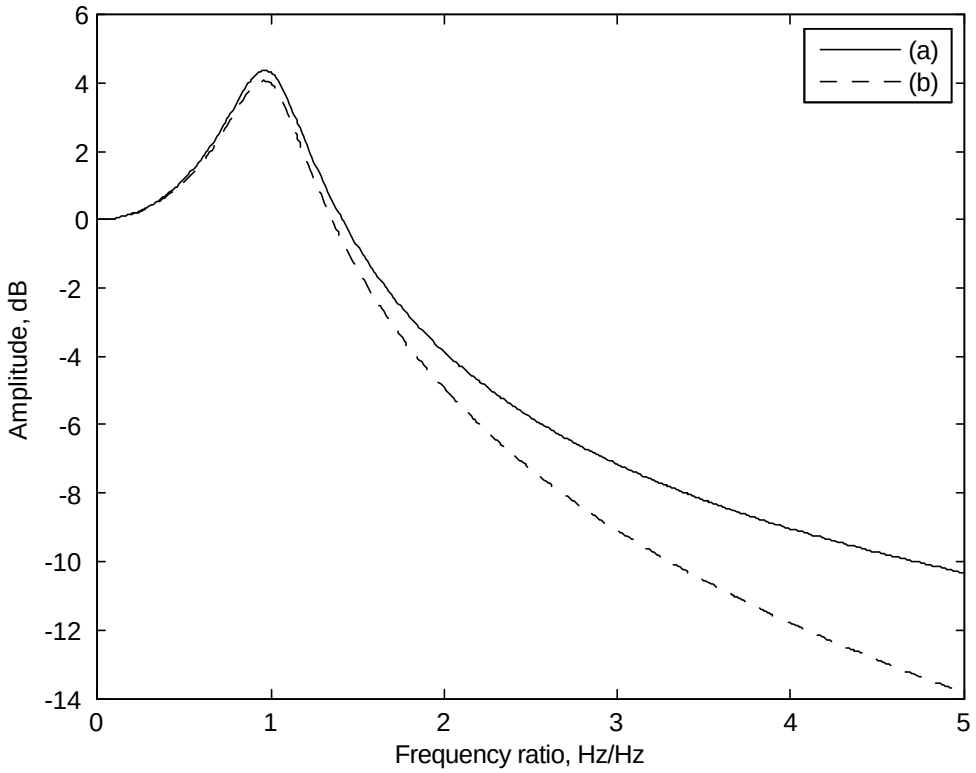

Figure 3.4: Transfer function amplitudes for systems (a) and (b).

The iterative search for parameters was concluded when each parameter deviation was less than 0.1% of its previous value, or $(\beta_i - \beta_{i-1})/\beta_i < 0.001$ for all β values.

3.6 Micro- to macro-scaling: Volume Averaging Technique

Numerical simulations were run on 35-by-40 μm segments of elastomer, which was 100-150 times smaller than the actual elastomers used in experimental results. Simulating a full-sized elastomer using the numerical simulation procedures here was not possible due to limitations in computing resources. To circumvent this, a volume-averaging technique was used to bound the range of expected elastomeric results. This section describes volume averaging techniques, and the methodology used to apply these techniques to this particular study.

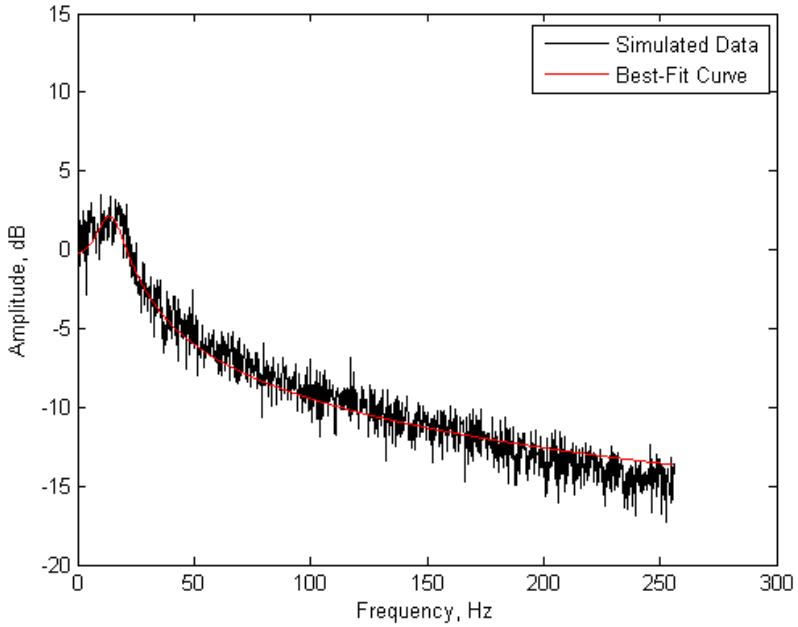

Figure 3.5: The numerically simulated transfer function for MRE30a is plotted against frequency and a best-fit line is found using Gauss-Newton least-squares algorithm.

A volume-averaging technique is used to extract meaningful macro-scale material characteristics from micro-scale behavior. The idea is that the effects of occlusions, point deformations, lamination, and other local microscopic behavior contribute to the overall macroscale material characteristics. For a given parameter x, the volume-averaged parameter $\bar{x}$ can be found such that

$$\bar{x} = \frac{1}{V} \int_V x dV, \tag{3.34}$$

where dV is the differential volume that x is valid for, and V is the volume of the overall material.

There is only one directional degree of freedom in the model discussed in this dissertation, that of longitudinal deformation. It was assumed that no deformation occured to change the cross-sectional area of either the individual nodes nor the overall simulated MRE. Therefore, Equation 3.34 can be simplified in this case such that an average parameter can

be found such that

$$\bar{x} = \frac{\sum_{n=1}^{N} x_n}{N}, \tag{3.35}$$

where N is the number of nodes, and x_n is the parameter value at the n^{th} node.

If the static relationship is considered between two nodes, such as those shown in Figure 3.6, that are directly in vertical alignment with each other, the equation of (non)motion can be found such that

$$k\left(x_i - x_{i-1}\right) = k\varepsilon_i = F_i, \tag{3.36}$$

where F_i is the 0th-order approximation of a magnetic force on that particle. Using the principle of volume averaging, Equation 3.36 becomes

$$k = \frac{\sum F_i}{\sum \varepsilon_i}. \tag{3.37}$$

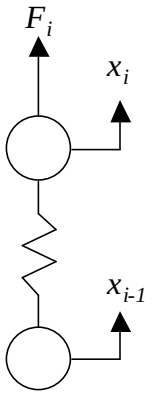

Figure 3.6: Two neighboring nodes are separated by a spring and magnetic force.

The stiffness reported in this work is the average stiffness among all the identified equations of motions. It is expected that as the number of chains decreases, the stiffness would also decrease. This is because there is less resistance associated with the magnetic chains, and more particles are able to move freely. As the MRE amplitudes increase and approach

all chains broken, the average stiffness should be the same as an MRE in the absence of a magnetic field.

CHAPTER IV

EXPERIMENTAL METHODS AND PROCEDURES

The experiments presented in this dissertation involved fabrication of MRE based vibration absorbers, and then evaluating their time-dependent response when subjected to an excitation. This chapter deals with the MRE mixing and curing process, the absorber and experimental apparatus, and procedures used to collect experimental data. The fabrication involved mixing and curing the MRE, and then attaching them to base and absorber masses. The assembled vibration absorber was attached to a shaker, with its coil controlled through a power supply. Both the shaker and power supply were manipulated to generate different absorber responses, which were measured.

MREs were mixed and cured to generate a desired volume fraction of iron, also referred to as iron concentration. An appropriate mass of iron micropowder, ISP Technologies Inc. grade R-1470, was added to RTV6186B, one of two parts of a GE Silicones elastomer, and mixed thoroughly. The second part of the elastomer, RTV6186A, was added drop-by-drop. The entire composition was mixed over a hot plate for five minutes. The elastomer mixture was poured into a mold and cured for thirty minutes. The mold was designed to elevate the elastomer temperature to over 90°C for thirty minutes as well as generate a magnetic field through the MRE to promote iron chain formation. The mold could produce one cylindrical MRE with overall diameter of 8 mm and 5 mm height.

The vibration absorber required two cured MREs, as well as an absorber mass and four pieces that attached together to form the base mass, as shown in Figure 4.1. Cured and cooled MREs were sliced in half lengthwise (cross-sectional areas were "D"-shaped) and glued to the absorber mass. Once the glue had dried, the opposite ends of the MREs were glued to the base mass.

The base and absorber masses were designed to minimize magnetic flux resistance around a desired magnetic path. Since the stiffness changes as a function of magnetic field, the

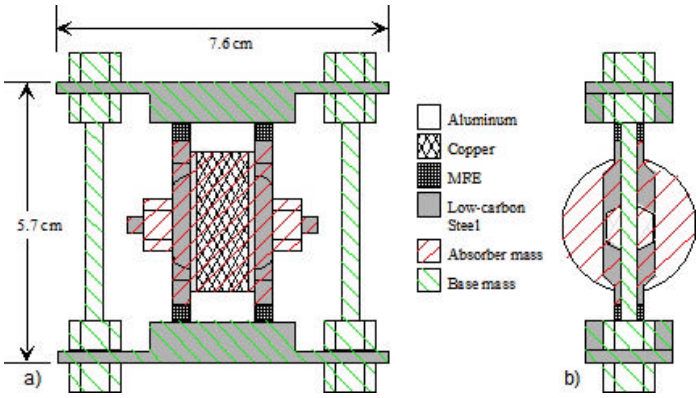

Figure 4.1: a) Front and b) side views of the base and absorber masses, connected with MREs. Materials were selected to minimize magnetic resistance around preferred flux paths.

absorber and base masses were designed so that maximum magnetic field would travel through the MREs. Figure 4.1 shows the materials used for each portion of the base and absorber masses.

The assembled SSA device was assembled in the experiment configuration depicted in Figure 4.2. A dSPACE DS1103 PPC controller board in a PC was used for data acquisition. The board sent a band-limited white noise excitation source to a Ling Dynamic Systems PA25E amplifier driving a Ling Dynamic Systems V203 shaker. A PCB type U288D01 accelerometer was placed between the shaker and the SSA device's base mass to find a uniform amplitude of excitation, and was powered by a Kistler 5134 power supply. The dSPACE board also sent a signal to a Kepco power supply, model 36-6D, operated in current mode. The Kepco supplied the current to the wire coil within the absorber mass that behaved as the magnetic field source. A Philtec remote-sensing D100-QPT displacement probe was rigidly connected to a base mass and measured the absorber's motion relative to the base mass. The SSA itself was aligned in two different configurations; in one configuration, the SSA was placed on top of the shaker, and excited parallel to the direction of gravity, and will be referred to as the "in gravity" case. In the other configuration, the shaker's motion input was perpendicular to gravity; that is, the SSA moved parallel to the ground, and any response was free of gravity's influence, labeled here the "gravity-free" case. The absorber mass and base mass were each elastically suspended to prevent out-of-plane motion for the

gravity-free configuration.

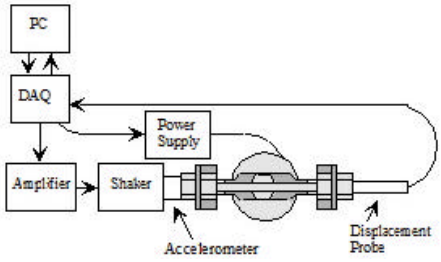

Figure 4.2: Experimental hardware arrangement for the absorber device. The absorber in this diagram represents an SSA suspended such that gravity was perpendicular to the direction of excitation.

The coil used in this experiment had a resistance and inductance of $R = 0.7$ Ohms and $L = 91$ mH, respectively. The power supply does not respond well to inductive loading; therefore, the load was placed in parallel with a capacitor $C_t = 0.1$ μF and resistor $R_C = 100$ kOhms, as indicated in Figure 4.3, to reduce electrical transients. Voltage across the terminals was measured, and the current I through the coil was identical to that supplied by the power supply, with a 95% settling time of 3.6 ms.

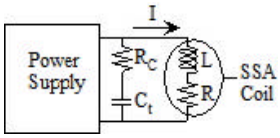

Figure 4.3: Transient suppression circuit, consisting of a resistor and capacitor, for power supply stability. R = 0.7 Ohms, L = 91 mH, C_t = 0.1 microF, and R_c = 100 kOhms.

While current input to the coil could be precisely regulated, the shaker input was dependent upon the amplifier settings, which could not be identically reset from test to test. To ensure that the shaker level was as similar as possible between tests, a 25 Hz pure tone signal was used to drive the shaker. The amplifier levels were varied until the accelerometer measured an rms value of approximately 0.015 V, where up to 6% deviation was tolerated test to test. This drive level was equivalent to approximately a 0.02 mm rms displacement excitation. Each MRE was excited at three different amplitude levels to check for any nonlinearities associated with displacement; the nominal excitation level, denoted as "A =

1.00", represented the 0.02 mm rms excitation level. An amplitude of "0.5" was 50% that level, and an amplitude of "1.50" was 150% of that level.

The SSA was subjected to controllably variable magnetic field levels under three different control schemes: steady magnetic field excitation, blind switching, and SSA switching. The purpose of these tests were to find static natural frequency levels, the characteristic response time under random switch conditions, and the characteristic response time under appropriate switch conditions, respectively. Once the amplitude level had been adjusted, the SSA was tested to determine the natural frequency of the SSA under steady magnetic fields. The time required to achieve the natural frequency under different switching cases was measured. The SSA wire coil was subjected to a static current load to produce steady magnetic field excitation. Both blind and SSA switching involved two step changes in magnetic field per test; the magnetic field was switched "on" and then "off" at specific instances. For blind switching, the magnetic field turned on precisely 1/3 of the way through the test duration, and then turned off at 2/3 of the way through. For the test condition calling for SSA switching, the magnetic field turned on at the first SSA-permissible time after 1/3 of the test duration had been run, and off 2/3 of the way through at the next SSA-permissible time. The SSA-permissible switch times, described in greater detail in Chapter II, are when $k_1 x_{rel}^2 = k_2 x_{rel}^2$, and when $\dot{x}_{base}(\dot{x}_{SSA} - \dot{x}_{base}) > 0$ to switch up, or $\dot{x}_{base}(\dot{x}_{SSA} - \dot{x}_{base}) < 0$ to switch down.

Testing was designed to examine the effects of switch condition, magnetic field, and amplitude level on MREs of different iron content. For each of these four test cases, six magnetic field levels were examined: 14, 28, 43, and 57 kG. These are the computed magnetic field at the center of the wire coil; it was estimated that the field at each MRE would be substantially less. Within each magnetic field level, three amplitude levels were tested to examine the interaction between magnetic field and displacements. Finally, each test case was repeated a total of nine times to assess the repeatability of these findings.

It is desirable to determine the usable frequency range of an SSA, quantified by the frequency shift ratio, FSR. The ratio of increase is calculated using the SSA's natural frequency in the absence of a magnetic field, and the percent increase in natural frequency

over the duration of the test data. Specifically, the FSR is calculated by

$$FSR = \left(\frac{\omega_{n,hi} - \omega_{n,0}}{\omega_{n,0}}\right), \tag{4.1}$$

where $\omega_{n,hi}$ is the natural frequency found in the field that yielded the largest natural frequency, which was at a magnetic field of 85 kG, and $\omega_{n,0}$ is the natural frequency in the absence of a magnetic field.

In order to glean information about transient behavior, an excitation input of a 30 Hz sine wave was used to obtain blind and SSA switching results. For each test, 1.5 seconds of data was accumulated at a sampling rate of 10 kHz. Two types of transient tests, involving the blind switching and SSA switching, were particularly challenging to evaluate. Fast Fourier transforms measure the frequency content of a signal throughout the entire duration; it cannot distinguish when particular frequency components were present in the time record. Wavelet analysis, and in particular the Wigner-Ville algorithm, has come into use to determine the time-frequency content of signals. While this was effective for broadband applications, it does not have the ability to distinguish between two mid-range frequencies that may change over time. Furthermore, broadband excitation appeared to mask any transient effect. The methods used to evaluate transient behavior are discussed in the next section.

4.1 Transient Analysis Procedure

Transient data and transient simulation results were analyzed by passing the data through a notch filter to separate the 30 Hz component of the response from the rest of the data. The filtered data was then analyzed to find the experimental response time. This section examines the rationale and validity behind these methods.

The experimental data was filtered to separate its forced response from its unforced, or transient response. If a mass behaves according to the equation of motion describing a mass-spring damper, such that

$$M\ddot{x} + Ke^{i\delta}x = F, \tag{4.2}$$

and a harmonic excitation of the form $F = \mathrm{Re}\left(fe^{i\omega t}\right)$, then the equation of motion can be broken down such that

$$M\ddot{x}_t + Ke^{i\delta}x_t = 0, \tag{4.3}$$

$$M\ddot{x}_f + Ke^{i\delta}x_f = \mathrm{Re}\left(fe^{i\omega t}\right) \tag{4.4}$$

where $x = x_t + x_f$, x_t is the transient response, and x_f is the forced response.

Equations 4.3 and 4.4 can be analyzed in the frequency domain to determine the amplitude and phase response of each component of the transient response. A general solution to Equation 4.3 is [28]

$$x_t = Xe^{(s+i\omega)t}, \tag{4.5}$$

where s is the real component of the response and ω is the harmonic response. Equation 4.5 is regularly manipulated to find rise times and settling times; the time is simply measured from the start of a vibration phenomenon until the first time when x_t is within some percentage of the final displacement for rise time, or else when x_t is always within some percentage of the final displacement for settling times [3].

This analysis did not yield productive results, however, because chains were continually breaking and reforming, meaning that the spring was in a constant state of transient response, and would not settle. Transient analysis instead was conducted by analyzing the forcing response.

The forced response can be found to be in the form $x_f = Xe^{i(\omega t+\psi)}$, where X is the amplitude, and

$$K = \frac{f}{X\left[\cos\left(\delta+\psi\right) - r^2\cos\psi\right]}, \tag{4.6}$$

$$\delta = \sin^{-1}\left(r^2\sin\psi\right) - \psi \tag{4.7}$$

where $r = \frac{\omega}{\omega_n}$. Figure 4.4 shows the normalized displacement of an absorber mass over time when placed in series with a 30% short (MRE30c) chain MRE. The displacement was normalized by the displacement achieved with one chain break, as described in equation 3.16. The "x", occurring 1.77 seconds into the simulation, denotes when the magnetic

field was switched on. The right-hand side of Figure 4.4 becomes a quasi-steady-state oscillation pattern more quickly than can be observed in this figure. Absorber amplitude was approximately 6.8 times larger in a magnetic field than absent a magnetic field, and the mean displacement in the magnetic field was 5.98e-5 m. Since the absorber amplitude in Figure 4.4 was larger when in a magnetic field than not, this SSA would suppress vibration in a base mass more effectively than its TVA counterpart at this operational frequency.

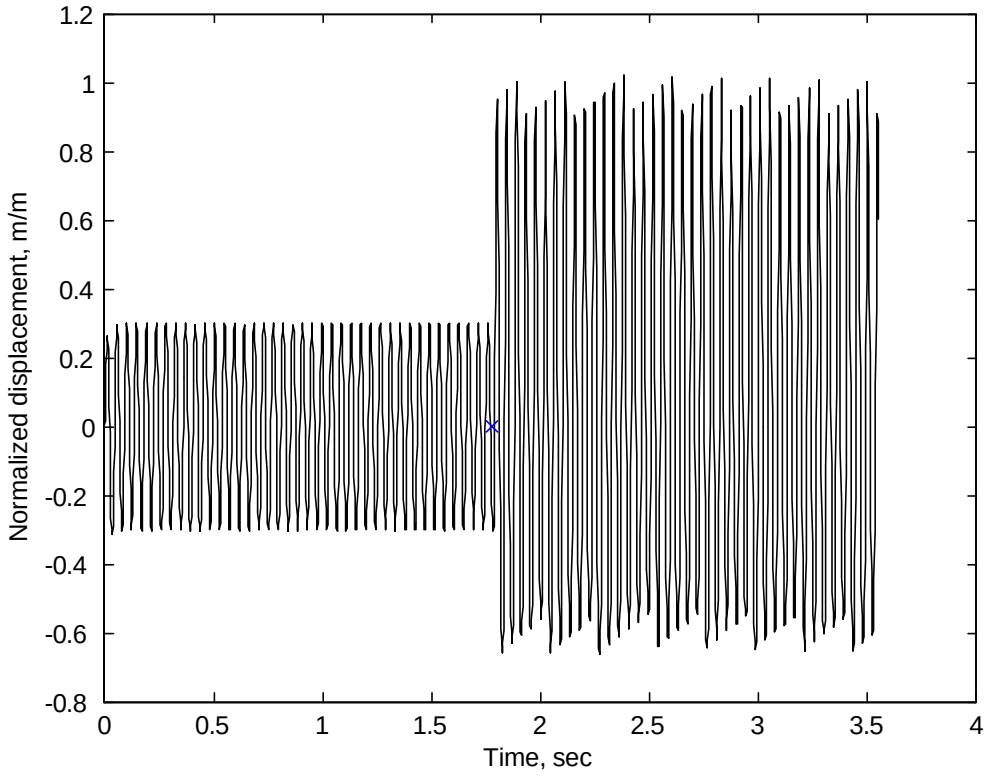

Figure 4.4: Absorber mass displacement is plotted against time. Magnetic fields were turned on at 1.77 seconds.

Figure 4.5 depicts the same data from Figure 4.4, but the x-axis was shortened so that the transient behavior at the point of the magnetic field change could be examined. The time at which the magnetic field was turned on was notated with an "x", and the beginning of quasi-steady-state behavior was notated with an "o". The transient time was found using the differences in amplitude and mean displacement. The characteristic response time was difficult to visually assess in Figure 4.5. It was clear that the characteristic response time

was shorter than the time to the first peak amplitude, occurring at roughly 1.8 seconds. The characteristic response time (CRT) was found instead by finding the root-mean-square amplitude for the steady-state post-switch displacement data, A_{rms}, and then finding the first data window that the root-mean-square amplitude across one cycle was within 1% of A_{rms}. The CRT was the time at which the beginning point in the data window occurs.

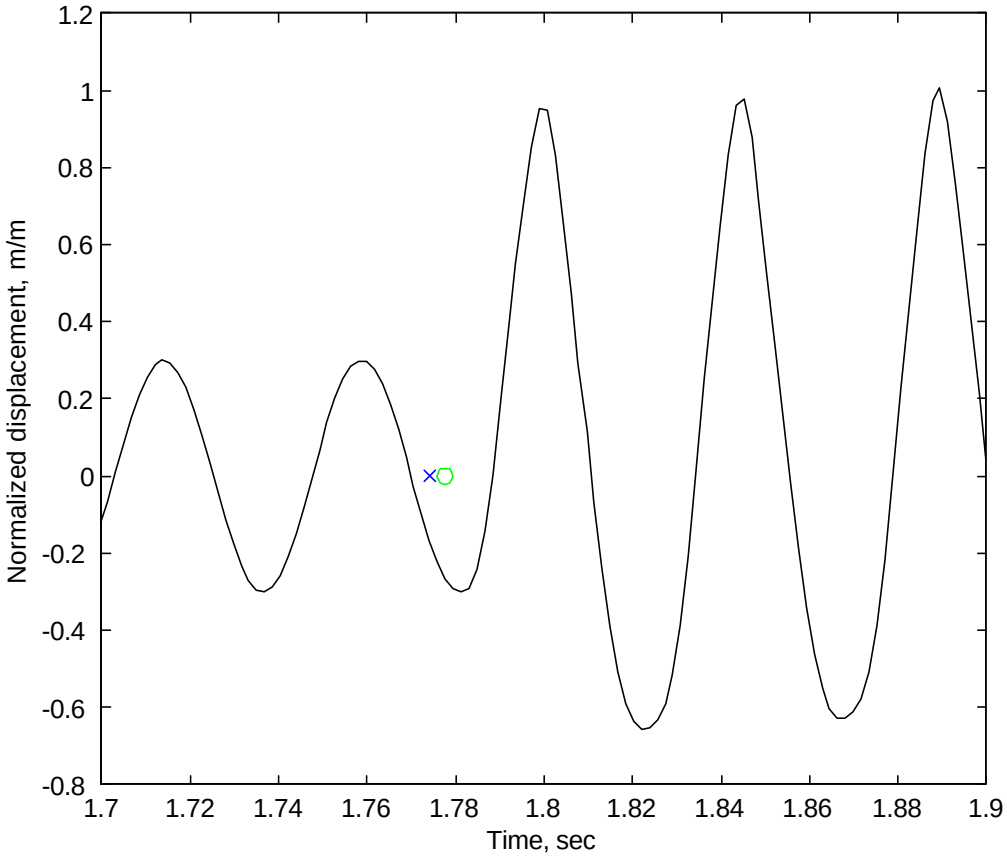

Figure 4.5: Displacement of the same 30% MRE as Figure 4.4 is magnified around the point of magnetic field step change.

The methods and procedures detailed in this chapter are used to acquire the data presented in the remainder of this dissertation. Four test cases are considered:

- the magnetic field was left at a constant level to find the "static" SSA behavior

- magnetic field stepped up or down at temporally fixed points to find the "blind switching" behavior
- magnetic field stepped up or down at the first SSA-algorithmically-permissible time after the temporally fixed points
- SSA is mounted either parallel to the magnetic field or perpendicular.

These four test cases and their results are discussed in Chapters V and VII.

CHAPTER V

MRES IN A STEADY MAGNETIC FIELD: SIMULATION AND EXPERIMENTAL RESULTS

Using the same general procedures as discussed in Chapter IV, MREs were studied under steady magnetic field but forced excitation conditions. Since the magnetic field was unchanging in these scenarios, these tests are referred to as "static" conditions, despite dynamic MRE behavior. MREs were simulated under different MRE sizes, static displacement ratios, and amplitude ratios. Select conclusions drawn from simulated behavior were compared with empirical data.

While the effect of excitation amplitude and static displacement levels is nonexistent for most springs within their elastic region, these considerations have considerable influence on MRE behavior in the presence of magnetic fields [32]. The excitation displacement used for this work was $x_{forcing} = [\text{rand}\,(t) + s]\,A \cdot dx$, where $\text{rand}\,(t)$ is an n-length vector of numbers randomly generated within the range of 0 to 1, s is the static displacement value, A is the amplitude ratio, and dx is the static distance required of the forcing displacement to just break every particulate magnetic bond.

Section 5.1 describes natural frequency behavior with different iron content, and compares that behavior to standard, accepted relationships between particulate content and natural frequency for $A = 1$ and $s = 0$. Section 5.3 discusses the effect of static displacement on natural frequencies in magnetic fields. Section 5.4 describes the effect of amplitude ratios on natural frequency, and compares to findings in the literature. Section 5.6 describes the effect of volume averaging on MRE as simulated MRE sizes approach those of experimental MRE sizes.

5.1 Natural Frequencies versus Iron Content: Simulation Results

Given that a baseline 5×6 configuration, as shown in Appendix A, predicts the natural frequency of a much larger MRE, the baseline 5×6 configuration was used to evaluate natural frequencies of MREs, excited at a forcing level that was such that $F = 0.01d$, where F is the forcing amplitude and d is the diameter of a simulated particles. In order to evaluate MRE performance in and out of magnetic fields, the non-dimensional frequency shift ratio was used, where

$$FSR = \frac{\omega_{n,hi} - \omega_{n,0}}{\omega_{n,0}}. \tag{5.1}$$

If the frequency ratio was larger than 0, the natural frequency in a magnetic field was larger than the natural frequency out of the magnetic field. An $FSR < 0$ value means that the natural frequency in a magnetic field was smaller than the natural frequency of the same device in the absence of a magnetic field.

Figure 5.1 presents the FSR for a) short chain MREs and b) long chain MREs subjected to a forcing ratio of 0 and an amplitude ratio of 1. While both figures demonstrate that MREs in longitudinal mode do indeed have positive FSRs, and that a natural frequency can as much as double between the field off and field on cases, there is a large difference between the relationship between iron content, FSR, and type of chain present in the MRE. Whereas the long chain MREs in Figure 5.1a) show an FSR versus iron content that is consistent with experimental data, shown in Figure 5.2, the short chain MRE behavior in Figure 5.1b) shows a more scattered pattern that is nonetheless dependent upon the inner short chain geometries.

Figure 5.1a) shows long-chain MRE behavior for MREs with iron content between 20% and 50%. Within the plot, there is a general trend of FSRs increasing as iron content increases, up through 40% iron content. The 50% MRE shows an FSR that is less than the peak FSR of the 40% MRE. A 40% long-chain MRE exhibited the largest FSR, where $FSR = 76\%$, which corresponds to a stiffness increase of 300%. The natural frequency of that MRE in the absence of a magnetic fields was found to be 10.2 Hz and the natural

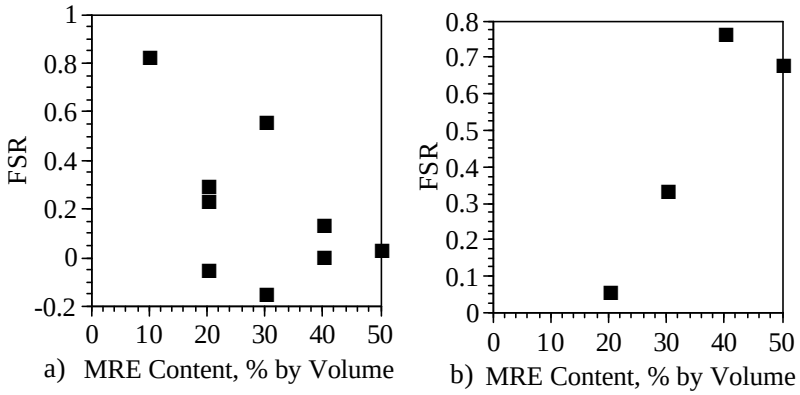

Figure 5.1: Frequency shift ratios of simulation a) short chain and b) long chain MREs excited with a forcing ratio of 1 and no static displacement.

frequency in the presence of a magnetic field was 18.0 Hz.

Figure 5.1b) shows short-chain MRE behavior for iron content between 10% and 50%. All but two elastomers exhibit positive FSRs, which means that natural frequencies when magnetic fields are turned "on" are higher than the natural frequencies of the MRE when there is no magnetic field. While most of the MREs exhibit positive FSRs, the values of FSRs vary greatly. The explanation behind this variation may be explained by the geometry of the particles within the MRE matrices themselves.

In order to explain the variation in short-chain MRE values shown in Figure 5.1, the internal structure of the short-chain MREs must be examined. For the purposes of this discussion, a node is in the "immediate vicinity" of another node if it is touching the first node, and no other node is between the two. A node in the immediate vicinity of a second node would appear in the second node's equation of motion. Consider the two negative FSR values, which correspond to MRE20b and MRE30b, shown in Appendix A. The structures of these two elastomers differ from the other elastomers in that the short chains do not have any other chains in the immediate vicinity of each other. Whereas the other MREs have short chains either next to each other, in the instances of MRE20b and MRE30b, the neighboring nodes are all elastomer. The other short-chain elastomers see quasi-long chain effects by virtue of these neighboring interactions, whereas theese two elastomer matrices do not benefit from these effects. However, the isolating-chain hypothesis does not hold

for the 10% MRE, which due to the small amount of particles, has a single chain. On the contrary, this MRE experienced the single largest FSR – an 82% increase. This data point leads to the conclusion that while geometry is highly important, there are perhaps more complex relationships that determine the FSR of an MRE.

The long-chain MRE FSR simulation presented in this section represent the experimental MRE behavior more faithfully than the short-chain MRE FSR simulation. While researchers have found that MRE particulate matter tend to form many short chains rather than long chains [6], the short chains also tend to cluster, forming long chain-like structures, as shown in Figure 2.2. In Figures 5.1a and b, it can be seen that while the short chain geometry leads to FSR results not necessarily consistent with experimental results, short-chain MREs with long chain-like structures follow the long-chain results much more closely, and are by extension more closely tied to experimental results. Future work would likely establish more close relationships between the short-chain MRE FSR behavior and long-chain MRE behavior by examining magnetic links cross-chain, discussed in Section 9.2. Given the results presented in this section, long chain MRE matrices are examined more thoroughly in subsequent chapters as most faithfully representing their experimental counterparts.

While the simulated responses did not mirror those of experimental work, these simulation responses are nonetheless relevant. These simulations represent a proof-of-concept that this type of modeling can be done to represent MRE behavior. Future efforts to refine property identification techniques would yield more consistent, and most likely relevant data with respect to experimental results.

The simulated data presented in this Section was compared to empirical data to determine the relevance of these simulation methods. Section 5.2 examines the relationship between empirical and numerical results, and the validity of this numerical technique is assessed.

5.2 Natural Frequencies versus iron content: a comparison to experimental results

The results described in Section 5.1 were compared to data that had been collected from a squeeze-mode vibration absorber device. Once the data is normalized according to static displacement, it is compared to the numerically simulated data discussed in Section 5.1. The experimental methods used to collect this data are discussed in Appendix B.

Experimental results from these tests are presented in Figure 5.2. The frequency ratios for the experimental results are much higher than those predicted by the numerical simulations presented in Figure 5.1. However, since the data is collected from a squeeze-mode device, a portion of the natural frequency change can be credited to the physical shape change in the MRE; that is, the static displacement length shortens in the presence of a magnetic field, and hence increases the stiffness and therefore the natural frequency of the MRE. The effect of such a shortening is examined in this section.

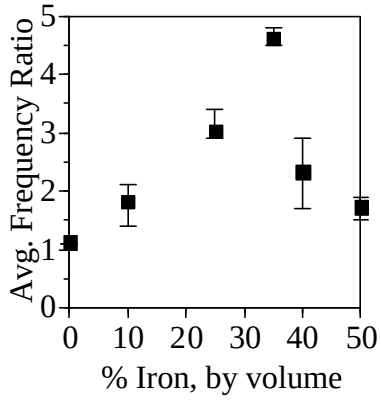

Figure 5.2: Frequency ratios of high magnetic field to no magnetic field, collected from a squeeze-mode vibration absorber.

As is discussed in Section 5.6, natural frequencies of elastomers are determined by

$$\omega_n = \sqrt{\frac{EA}{LM}}. \tag{5.2}$$

The elastomer is assumed to have a uniform cross-section, such that the volume $V = AL$. Using this assumption for volume, Equation 5.2 is rewritten such that $\omega_n = \frac{1}{L}\sqrt{\frac{EV}{M}}$, hence

$$E_{hi} = \frac{\omega_n^2 M L_{hi}^2}{V}', \tag{5.3}$$

where E_{hi} and L_{hi} are the Young's modulus and elastomer lengths with an applied magnetic field. The lengths of the elastomer are determined by the static equilibrium equations of motion

$$K_{hi}\left(L_{hi}-l_0\right)+F_m-Mg=0 \tag{5.4}$$
$$K_0\left(L_0-l_0\right)-Mg=0,$$

where l_0 is the elastomer's unstretched length, and F_m is the attractive force imposed on the absorber mass by the magnetic field. F_m is the separation force,

$$F_m=\frac{nB^2A}{2\mu_{rel}\mu_0}=\frac{nB^2V}{2r\mu_{rel}\mu_0}, \tag{5.5}$$

where $r=L_{hi}-l_0$ and n is the number of particles separated. Using the Fröhlich-Kennelly equation, where

$$\mu_{rel}=1+\chi=1+\frac{\left(\mu_r-1\right)m_s}{m_s+\left(\mu_r-1\right)H}, \tag{5.6}$$

and $\mu_r=10$ and $m_s=1.5\times10^6$ A/m for iron, m is known to be $m=\mu_0\chi Hv$, where v is the volume of a particle, F_m can be recalculated as $F_m=\left(\phi d^3\mu_0\chi^2\right)/\left(8\mu_{rel}\right)H^2$. Substituting this expression for F_m in Equation 5.4 yields a fourth-order polynomial in terms of L_{hi}, whereas $L_0=l_0+g/\omega_n^2$. Although four roots can be found to this fourth-order equation, only one root will be exclusively real and negative; this is the physical value for the static displacement. The value for E_0 can be found by rearranging Equation 5.2 and using experimental data for ω_n. Once these variables have been computed, E_{hi} can be calculated from empirical data using Equation 5.3.

The empirical $\omega_{n,hi}$ is compared to a theoretical $\omega_{n,hi}$, assuming that there is no change in Young's modulus, and only the change in static displacement affects the MRE. Empirical data is collected according to protocol discussed in Appendix B, and then the percentage deviation is calculated as

$$\text{deviation}=\frac{\omega_{n,empirical}-\omega_{n,theoretical}}{\omega_{n,empirical}}\times100\%. \tag{5.7}$$

A positive deviation indicates that the empirical data exhibited a larger natural frequency change than would be predicted if the natural frequency change were due only to the change in static displacement length.

Figure 5.3 shows the percentage deviation as a function of magnetic field for seven different MRE formulations. A 0% MRE showed a 16% decrease in natural frequency over what would have been expected from pure change in static length alone; while this indicates that the theory does not accurately predict empirical outcomes, every other MRE in Figure 5.3 shows more than a 16% increase in natural frequency. Therefore, regardless of the shortcomings in predicting static displacement and its effects on natural frequency, MREs consisting of at least 10% iron (or more) show substantive natural frequency increases that can not be accounted for by an enlarged area and decreased length.

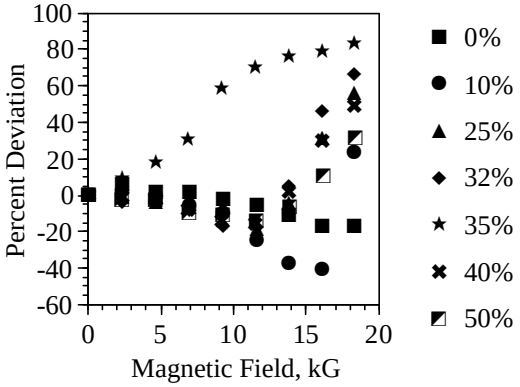

Figure 5.3: The percentage each MRE composition deviates from the expected performance is shown in different magnetic fields.

The simulation results presented in Figure 5.1 are similar to the empirical data presented in Figure 5.3 in that they both predict a maximum natural frequency change between 30% and 40%. The simulation results provide an explanation for the results that are seen in Figure 5.3

5.3 The effect of static displacement on natural frequency

In classic vibration theory, static displacements are the consequence of static forces, and that is the only effect a static force can induce. However, once magnetic fields are introduced, the effect of a static displacement could conceivably prevent MRE particles from generating magnetic bonds, or conversely, prevent large enough motion to break these bonds. The purpose of this section is to examine the effect of static displacement on MRE behavior.

The effect of static displacement was simulated on the MREs referenced in Appendix B, and the results are shown in Figure 5.4. The MRE was subjected to random excitation and static displacement ratios r_{sd}, which was related to the static displacement, Δ, as $r_{sd} = \frac{\Delta}{d}$, where d was the diameter of a particle. A negative static displacement percentage indicates a net compressive MRE state, and a positive static displacement ratio indicates the MRE was in tension. Short-chain MREs exhibited a few negative FSR values, primarily when the static displacement was forcing a compressive states. Long-chain MREs exhibited only positive FSR values.

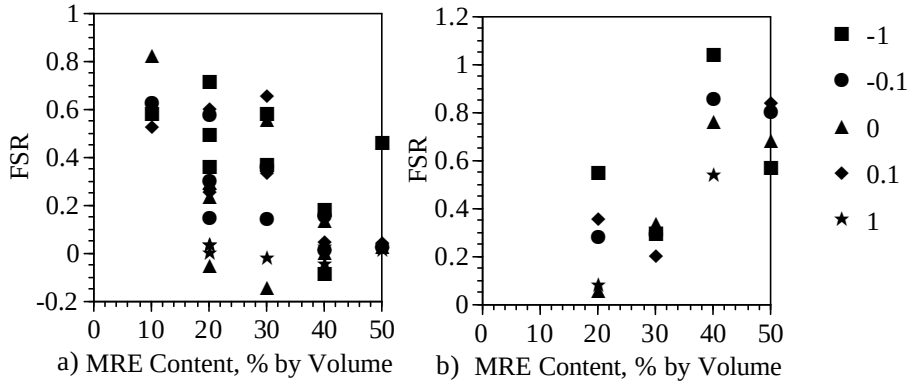

Figure 5.4: Frequency shift ratios of simulated a) short chain and b) long chain MREs versus MRE content for different static displacement ratios.

From Figure 5.4b), it can be seen that regardless of static displacement, the peak FSR value is achieved with long-chain MREs when the iron content is 40%. While the individual plot points on this figure vary according to static displacement, the overall trend of lower FSRs at 20% and 50% are also preserved. Upon examining Figure 5.4a), no trend is apparent among either iron content or static displacement. The conclusion that is drawn from these results is that this model is not able to adequately capture the effect of static displacement on natural frequency.

It is unsurprising that this model is unable to capture static displacement effects on natural frequency, as this model does not include the geometric deformation of the matrix in response to compression or tension, nor does it include material laminiation effects or local strain responses to occlusions, all of which would affect natural frequency. Despite

this deficiency of the model, prediction of static displacement effects was secondary to the goals of predicting unstrained MRE parameters and transient results. Further refinements to the model can be included at a later date to more adequately predict the effect of static displacement on MRE vibration parameters.

5.4 Forcing amplitude effect on natural frequency: simulation and experimental results

MREs have been empirically found to exhibit increased natural frequencies in the presence of magnetic fields, but only for limited ranges of forcing amplitude levels [6, 32], and theoretical studies have yielded the same conclusions [40, 33, 7]. The work presented in this section describes the range of amplitude excitation on the upper and lower bounds for MRE response.

MRE behavior was simulated under variable displacement amplitude conditions. Forcing amplitudes were simulated in comparison to the diameter of a ferromagnetic particle, such that a forcing amplitude of 1 meant that the amplitude was equal to the diameter of a ferromagnetic particle. MREs were evaluated both in and out of a saturated magnetic field, and natural frequencies were calculated according to the least squared error method.

Figure 5.5 displays the average frequency ratio for each simulated MRE against the excitation amplitude coefficient. A simulation value of "1" represents the minimum forcing excitation required to cause every chain to break. An amplitude ratio of 1 yielded the largest FSRs, with the peak value of 0.76 occuring with a 40% MRE. As the amplitude ratio increases beyond 1, the FSR decreases and approaches 0. This is consistent with both the experimental and theoretical explanation for this behavior, and further validation of the appropriateness of this model. This finding is an important contribution, because whereas others have found these results experimentally or by studying a homogeneous composition using FEA simulations, this is the first model that examines particulate and elastomer contributions as an aggregate.

The further implications for this decreasing FSR increase in the face of increasing amplitude is that MREs offer increasingly limited benefits for large-amplitude excitations.

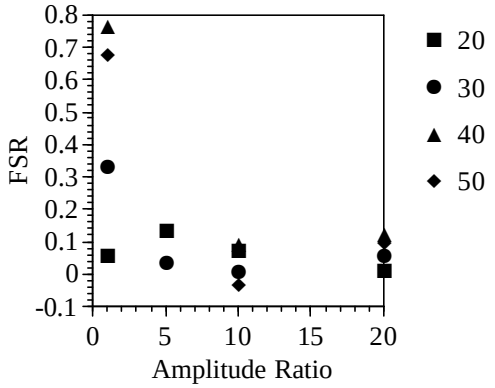

Figure 5.5: Frequency shift ratios for simulated long-chain MREs at four forcing ratios.

This means that while MREs may be a beneficial choice for variable stiffness applications, this will only hold true if the amplitude of excitation is known to be below a threshold value. Conversely, MREs would not be an appropriate choice for disturbances that can not be necessarily known to hold to this restriction.

5.5 Frequency Shift Ratios versus Magnetic Field: Simulation and Experimental Results

Magnetic field strength was varied to examine the effect on MRE motion. This was a particularly valuable study, as magnetic field strength is a controllable element for an SSA user to obtain desired behavior. MRE behavior was simulated using the numerical model. Magnetic field strengths are reported in terms of percentage iron saturation in the MRE chains.

Figure 5.6 shows the average natural frequency across many MREs for magnetic fields that were 25%, 50%, 75%, and 100% of the saturation magnetic field. The natural frequencies for MREs subjected to 25%, 50% and 75% of the magnetic field saturation did not show statistically significant deviations from lower and no-field natural frequencies. However, there is greater than 97.5% certainty, using a Student's t-test analysis, that the 100% saturation magnetic field yields larger natural frequencies than those of lesser saturation.

Figure 5.7 shows FSR results for MREs excited in squeeze-mode. It can be seen that for MREs of all iron content except 32%, FSR values are close to zero for any field value less than

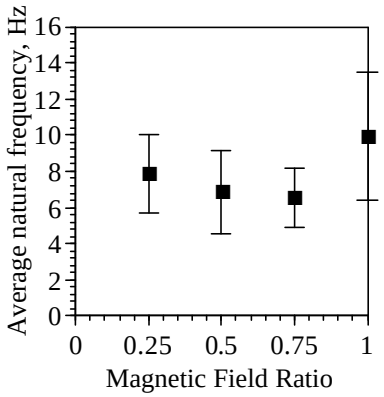

Figure 5.6: Average CRTs for MREs subjected to varius forcing frequency ratios when the magnetic field is 25%, 50%, 75%, and 100% saturated.

12 kA/m. On the other hand, FSRs increase for most iron content values above the 12 kA/m value. This is consistent with the simulation finding in Figure 5.6 that there is minimal natural frequency increase below total magnetic field saturation. Since the simulation predicts no FSR change below a threshold value between 75% and 100% saturation, and experimental results indicate the same, it can be concluded that the simulation is able to correctly predict the magnetic field level at which the frequency can be expected to shift.

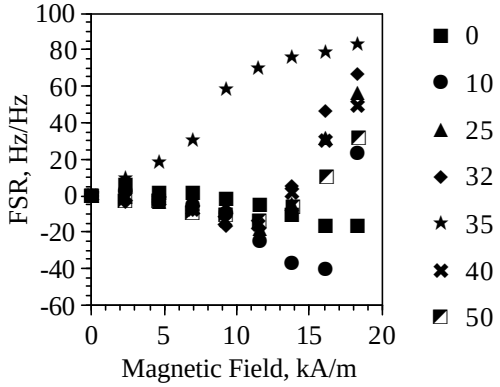

Figure 5.7: FSRs are plotted against magnetic field for seven different MRE compositions.

5.6 Simulation Results: Natural Frequencies and Scaling Effects

The MRE responses to steady magnetic fields reported in the previous three sections were simulated according to the procedures set forth in Chapter III, and using MRE blocks with length and area multiplication factors of 1. Simulation MREs were examined on a microscopic scale not representative of common MRE sizing. Each block needed to be scaled 145×108 times in order to be the same size as the experimental MREs. As this would have required more computing power than was available, the method of volume averaging, as described in Section 3.6, was used to determine the average stiffness for each node within the numerically-simulated MRE when it was scaled appropriately first for the proper area, and then for the proper length.

Figure 5.8 shows the averages stiffness for each node within an MRE as a function of scaling factor when scaled over MRE a) length and b) width. When stiffness is volume-averaged over the scaled length, the stiffness decreases exponentially as a function of the scaling. When scaled over the area, the stiffnesses settled towards a non-zero number. This means that the average stiffness-per-unit-node can be found to be between 5.9×10^{-3} and 2.83×10^{15} N/ $\left(m \cdot unit^2\right)$ for a 20% MRE, above 318 N/ $\left(m \cdot unit^2\right)$ for a 30% MRE, and 4.2×10^{-4} and 168 N/ $\left(m \cdot unit^2\right)$ for a 40% MRE.

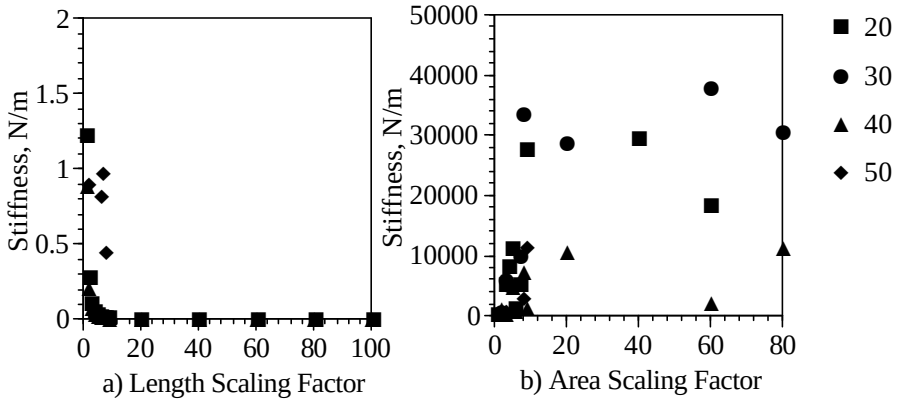

Figure 5.8: Average stiffness values for scaling over MRE a) length and b) width for long-chained MREs.

A similar method was used to find the overall natural frequency of the MRE and its

absorber mass for the expansion. Figure 5.9 shows the natural frequency of MREs as they are scaled over a) length and b) area. The average natural frequency for a full-sized MRE could be estimated to be between 0.07 Hz and 762 Hz.

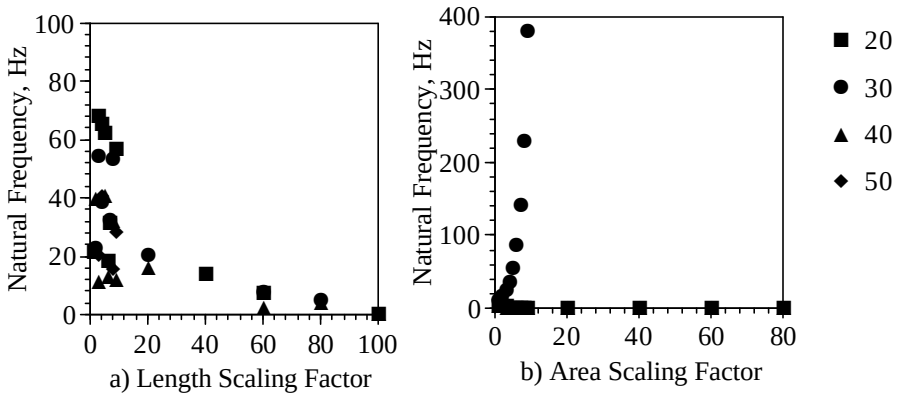

Figure 5.9: Natural frequencies are found for long-chain MREs scaled up by a) length and b) area.

CHAPTER VI

MRES IN A TRANSIENT MAGNETIC FIELD

Whereas steady-state behavior described in the previous chapter was found by using random excitation, transient behavior was assessed in simulation by exciting micro-MRE models harmonically in a variable magnetic field. The absorber mass's displacement was calculated, and its oscillation patterns were observed. While MREs in magnetic fields do not have "steady-state" behavior per se, they do exhibit repetitive oscillation patterns that can be described as quasi-steady-state. Section 6.1 describes how MRE transient behavior is assessed. Section 6.2 characterizes the transients as a function of iron content. Section 6.3 characterizes excitation amplitude. Section 6.4 characterizes excitation frequency, and Section 6.5 measures the effect of magnetic fields turning on versus magnetic fields turning off. Section 6.5 characterizes magnetic field strength.

6.1 Assessing transient behavior

MRE models were simulated such that the bottom row was subjected to a 40 Hz oscillation. The amplitude of oscillation was $A = n\,(dx)$, where n was the number of possible chain breaks and dx was the displacement associated with a single chain break. The top row of each MRE was attached to an absorber mass, and this mass's displacement was computed in order to assess transient behavior.

For the purposes of this dissertation, transient behavior is defined as the variation of motion in an absorber mass as a direct result of the addition or removal of a magnetic field. In this work, if a magnetic field had previously been absent and was added in a stepwise manner, this change in magnetic field is referred to as turning on. If, on the other hand, a magnetic field is present, and instantaneously removed at a specific instant in time, that is referred to as turning off the magnetic field. All changes in magnetic fields are assumed to be instantaneous. Each test case and simulation was run nine times, and average values

are reported in the remaining sections.

The ratio between the pre- and post-switch rms-amplitudes and the CRT analysis are the basis for comparing the effects of iron content in Sections 6.2, 6.3, 6.4, 6.1, and 6.5.

6.2 The effect of iron content on transients

Simulation MREs were excited harmonically and CRTs were compared by iron content. Figure 6.1 shows average CRTs for MREs when a magnetic field is turned on and when a magnetic field is turned off. For long-chain MREs, shown in Figure 6.1a, the CRT response is longer when magnetic fields are turned off. When a magnetic field is turned on, according to SSA switching behavior, the MRE must be undeformed, and therefore not in any strain situations. Individual particles instantly create a chain with their neighboring particles. The long chains connect the base mass to the absorber mass, and hence the absorber mass will instantly be forced into the same motion as the base mass – and hence no CRT. On the other hand, when the magnetic field is turned off, the chains are dissolved and the absorber mass will behave in a manner consistent with its transient behavior.

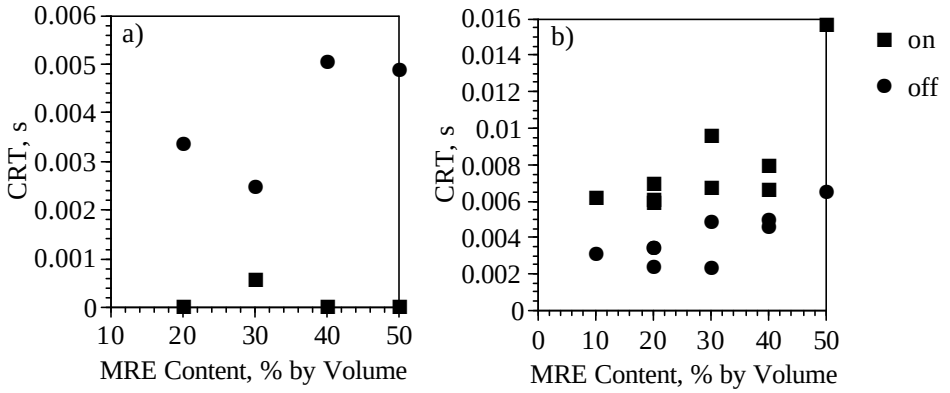

Figure 6.1: CRTs for simulated a) long-chain and b) short-chain MREs of different iron content, for magnetic field conditions changing to on and off.

Short-chain MREs exhibited the opposite effect, which makes sense because the chains do not connect the forcing motion of the base to the absorber motion. However, that is also a weakness in the modeling of the short chains, and one that does not reflect reality, as discussed in Section 5.1. Therefore, short chain MRE behavior will not be examined in

this chapter.

In addition to long- versus short- chain deviations in CRT behavior, CRTs also vary linearly with iron content. This is a logical result, as an MRE with more iron content has more potential chains to break, and thus can go through more transitional period before settling into a quasi-steady state oscillation pattern.

6.3 The effect of step changes in magnetic field and excitation amplitude on transients

This section describes CRT behavior in terms of step changes in the magnetic field, which is referred to here with the "on" and "off" nomenclature, and excitation amplitude. As was discussed in Section 6.1, excitation amplitude was measured in terms of number of chain breaks, and the displacement associated with each chain break. Simulation results are discussed and then compared to experimental tests.

Figure 6.2 shows average CRTs when magnetic fields were turned off across long-chain simulated MREs subjected to amplitude ratios between 1 and 20. Figure 6.2a shows CRT plotted against MRE content, which reveals the much lower CRT values for the 30% MRE. Figure 6.2b shows the CRTs plotted against ratio of amplitude excitation. In this plot it is much clearer that amplitude of excitation very much affects CRTs, and not necessarily in a linear fashion. The conclusion to be drawn here is that MRE-based vibration absorbers exhibit excitation amplitude-dependent transient characteristics in the numerical simulations.

Figure 6.3 shows average CRTs for MREs placed in the experimental SSA described in Chapter IV and subjected to different excitation amplitudes, and separated by whether they were subjected to an "on" or "off" magnetic field.

By comparing the transient times in Figure 6.2 to Figure 6.3, it can be seen that despite the different CRT time frames (8 - 16 ms for the simulation, 0.49-0.51 s for the experiment), CRTs are independent of excitation amplitude, and CRTs are larger when a magnetic field is turned "off" than "on". The implication is that the natural frequency response of the simulated MRE-based SSA is closer to the forcing frequency when the magnetic field is on

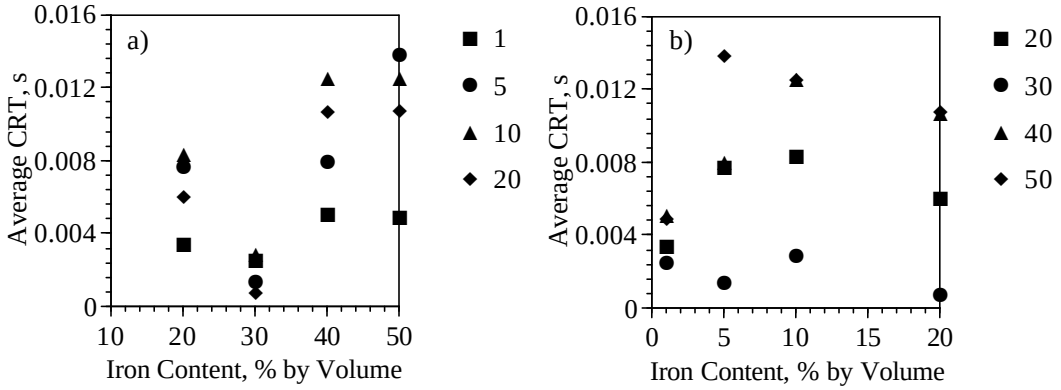

Figure 6.2: Average CRTs for simulated MREs subjected to a) different excitation amplitude ratios, and b) differentiated by a magnetic field being turned "on" or "off".

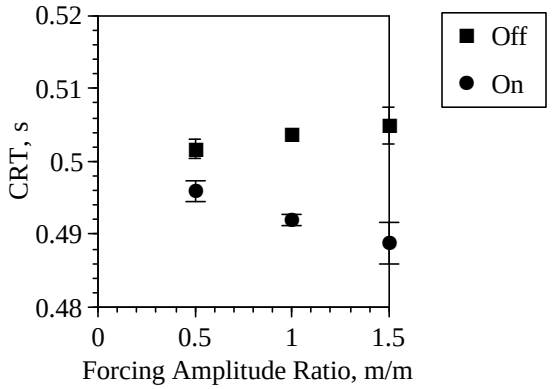

Figure 6.3: Average CRTS across experimental MRE data at different forcing amplitude ratios for magnetic fields being turned "on" and "off"

than when it is off; this is confirmation that the MRE-based SSA experienced a natural frequency shift. Since the amplitude of the SSA is higher when the magnetic field is turned on, this means that the SSA device is able to "absorb" more energy when the magnetic field is on, if the device is excited at the listed forcing frequency.

To confirm that the discrepancy between the magnetic fields turning on and off is not an aberration, voltage was measured across the magnetizing coil on the SSA, and the difference between the time response of the voltage when rising or falling was negligible. The cause of the difference in CRTs is due in part to the hysteretic effect of magnetism (please refer to Section 2.4 for a description of this phenomenon), and partially due to equation of motion mechanics. While the MREs present in the experiment could have been affected by either

phenomenon, hysteretic effects were ignored in the simulation. Therefore, the discrepancy in CRTs must be due to structural mechanics.

As a further explanation, consider a chain of ferromagnetic particles. Each particle engages in motion unrelated to its neighbors in the absence of a magnetic field. Once a magnetic field is applied, the attractive forces compel each particle to align and begin motion as a partial or entire chain. On the other side, consider the effect of a magnetic field being turned off once each particle in a chain is moving together at a common velocity. While there is no longer any force compelling these particles to remain aligned, they will continue to move together for the very short term due to the effects of inertia.

6.4 The effect of excitation frequency on transients

Excitation frequency plays a significant role in the ability of a TVA to suppress vibration. A TVA exhibits its maximum amplitude at its resonance frequency, which is slightly lower than its natural frequency. SSAs also can be characterized as single-degree-of-freedom vibration absorbers with a natural frequency.

Unfortunately, an SSA's performance when subjected to random excitation does not necessarily predict pure-tone responses for SSAs. SSAs are time-varying systems, since every time a chain is broken or created, transient oscillations ensue. On the macro scale level, these transient oscillations manifest themselves as increased energy loss, friction, loss factor, or some other damping property. However, because the macro scale MRE would be subjected to ongoing state changes, regardless of the forced frequency oscillation, there will be ongoing, thus sustained transient oscillation response, hence the "quasi-steady-state" term from the beginning of this chapter.

MRE transient behavior was examined as it related to excitation frequency in a pure-tone oscillation. Figure 6.4 shows CRTs for a) magnetic fields that were turned on and b) magnetic fields turned off for long-chain MREs at various forcing frequencies. In general, the CRT required when the magnetic field was turned on was less than the CRT required when the magnetic field was turned off.

In order to better compare CRTs with magnetic fields being turned on versus off, the

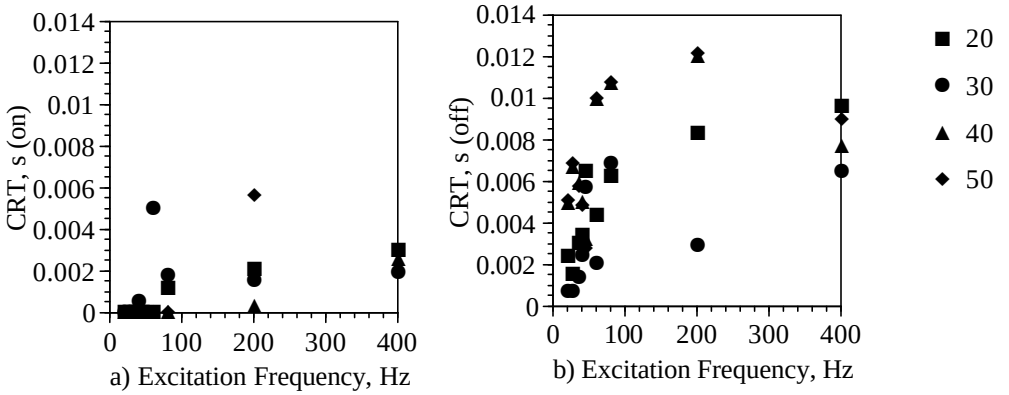

Figure 6.4: CRTs for a magnetic field being turned a) on and b) off versus forcing frequency.

difference between the CRTs, calculated as

$$\Delta CRT = CRT_{off} - CRT_{on}, \tag{6.1}$$

was plotted against MRE iron content in Figure 6.5. Any ΔCRT that is greater than 0 has a CRT_{off} that is greater than its CRT_{on}. It can be seen that for all but a few data points, $CRT_{off} > CRT_{on}$. Referring back to Figure 6.4, it can be seen that many CRT_{on} values are equal to zero.

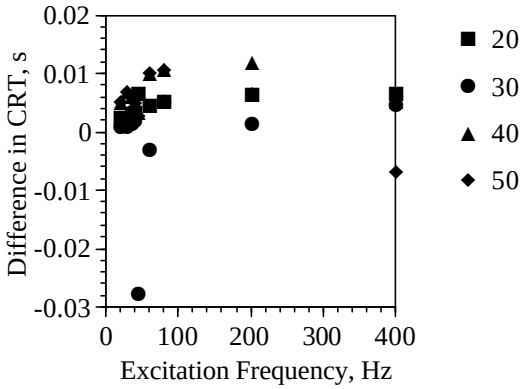

Figure 6.5: Differential CRTs are plotted against excitation frequency for long-chain MREs.

There is a physical explanation for the differential CRTs demonstrated in Figures 6.3, 6.4, and 6.5. When a magnetic field is turned on when there is no strain across an MRE, in accordance with the SSA algorithm, the presence of a magnetic field causes chains to instantaneously form, and there is effectively no transient – the entire chain is forced to move

in alignment. However, when a magnetic field is turned off, iron particles will separate according to the forces exerted on them, which means that the transients will be related to the damped natural frequency of the individual particles – and hence nonzero. Figure 6.3 demonstrates that this phenomenon also exists experimentally. This means that different input shaping may be required to optimize magnetic field shut-off CRT response as opposed to magnetic field turn on CRT response.

In order to assess the meaning of these CRTs, it was useful to recall, from Section 2.1, that CRT must take less than a 1/4−period if an SSA's performance was to be stable [20]. Figure 6.6 plots the maximum allowable excitation frequency for each forcing frequency ratio to ensure stability was maintained. The maximum allowable excitation frequency, occurring for a 1.1 forcing frequency ratio, was 250 Hz. Allowable excitation frequencies decrease as the distance above the natural frequency increases.

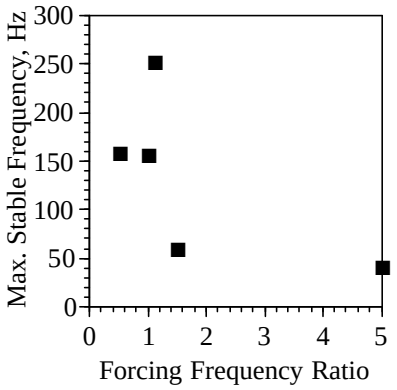

Figure 6.6: The maximum allowable equivalent natural frequency is plotted against the forcing frequency ratio to ensure a stable SSA response.

While this finding seemingly limits design properties of an MRE considerably, it is possible that looser transient limit standards could in fact yield stable results. While beyond the scope of this work, future study could determine the precise properties of the stability limits of MRE-based ATVA and SSA devices.

6.5 The effect of magnetic field strength on transients: simulation results

Magnetic field strength was varied to examine the effect on MRE motion. This was a particularly valuable study, as magnetic field strength is a controllable element for an SSA user to obtain desired behavior. MRE behavior was simulated using the numerical model. Magnetic field strengths are reported in terms of percentage iron saturation in the MRE chains.

Figure 6.7 shows the CRTs for long-chain MREs when the magnetic fields were turned off. (CRTs for magnetic fields being turned on are not reported, as there were primarily no CRT times for magnetic fields being turned on. For an explanation of why that is, please see Section 6.2.) The magnetic field ratio was normalized to 1 for full magnetic saturation. While each MRE has a different CRT value, the CRT value is unaffected by magnetic field ratio.

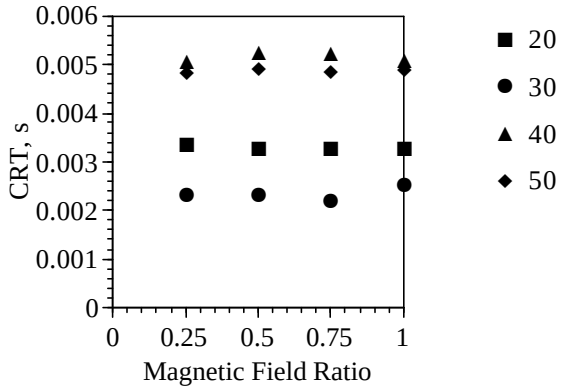

Figure 6.7: CRTs versus magnetic field ratio for long-chain MREs subjected to a magnetic field being turned off.

Because the CRT is insensitive to different magnetic field levels, the characteristic response time can not be controlled by a positive magnetic field. Therefore, MREs are not controllable using input shaping. This means that if it is desirable to implement an SSA algorithm and MREs do not meet the performance requirements, then MREs should not be utilized in that particular application.

It may still be possible to use MREs in this particular scenario. This work delved

exclusively in the realm of a positive magnetic field. The effect of a reversed magnetic field – one where the magnetic poles were switched – was not studied. It is possible that in such a configuration, either the change in polarity or else the hysteretic phenomenon inherent in iron could be exploited to give the control desired.

CHAPTER VII

DAMPING COEFFICIENTS

While the primary thrust of this work is on the effect of the magnetic field on a stiffness change, its effect on damping cannot be ignored. Damping coefficients' dependencies on magnetic field affect not only the ability of the SSA to effectively suppress vibration, but also the efficacy of the SSA switching laws discussed in Chapter III. This chapter explores simulated damping, and the results associated with extrapolating the simulation responses to a scale on par with macro scale MREs.

The equation of motion governing a mass subjected to a complex spring is found to be

$$\ddot{x} + 2\zeta\omega_n\dot{x} + \omega_n^2 x = \frac{F}{M}. \tag{7.1}$$

If the forcing excitation, F, is harmonic, then the displacement is

$$x = Xe^{i(\omega t+\psi)}, \tag{7.2}$$

where ψ is the phase lag. Using a nonlinear Gauss-Newton method discussed in Section 3.5, the damping coefficient was found.

This chapter is devoted to studying the damping coefficient, ζ. It has been assumed that the damping coefficient is unaffected by the presence of a magnetic field, which is why MREs are classified as smart springs rather than smart dampers. The data reported in this section was collected via numerical simulation, and were found using the Gauss-Newton least squares algorithm concurrently with the natural frequency data reported in Chapter 5. The effect of iron content is discussed in Section 7.1, excitation amplitude in Section 7.2, and static displacement in Section 7.3.

7.1 The effect of iron content on damping coefficients

Damping coefficients were compared between simulated MREs with different iron content. Figure 7.1 shows damping coefficients for MREs with 10-50% iron content and no static

displacement for MREs with a) long and b) short chains. Damping coefficients for long-chain MREs, shown in Figure 7.1a, exhibited that when magnetic fields were turned on, coefficients were roughly double their non-magnetic-field counterparts for all MREs except the 30% MRE. Short-chain MREs did not exhibit any significant deviation, which is what would be expected.

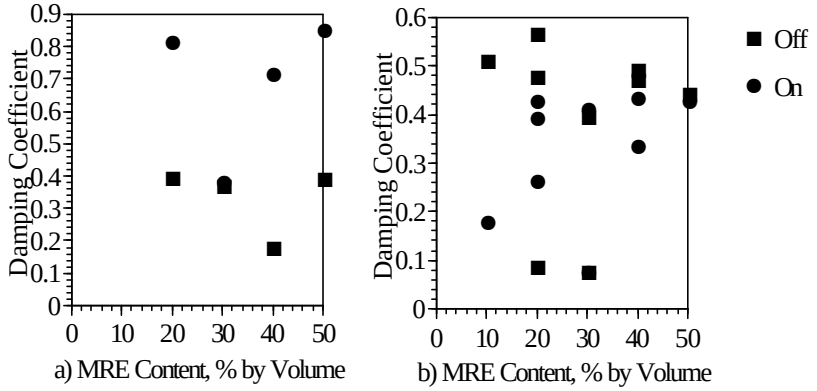

Figure 7.1: Damping coefficients are plotted against MRE content for a) long chain and b) short chain MREs with magnetic fields on and off.

Since the peak frequency response is a function of both natural frequency and damping coefficient, the results shown in Figure 7.1 raises the question, is the peak frequency shift actually due to damping switching rather than stiffness shifting? Realizing that the peak resonant frequency occurs at a value less than the natural frequency, and that the larger the damping, the lower this peak frequency would be, it follows that the increased damping coefficients for the magnetized MREs would cause natural frequencies to be lower if the same peak frequency was observed. However, the opposite was observed; while there is increased damping when the magnetic field is turned on, there were also increased natural frequencies. Therefore, there is still a legitimate stiffness increase phenomenon.

7.2 The effect of amplitude on damping coefficients

Excitation amplitude was shown to affect natural frequency in Section 5.4. Figure 7.2 shows damping coefficients for a) long and b) short chain MREs subjected to different amplitude ratios. An amplitude ratio of "1" indicates the minimum amplitude to ensure

every chain bond breaks. While short-chain MREs show scattered damping coefficient patterns not correlated to either iron content or amplitude, the long-chain MREs do have amplitude-dependent damping ratios. Figure 7.3 shows long-chain MREs' damping coefficients at different amplitude rates. As the amplitude ratio approaches 20, the damping ratio approaches 0.4, which is the value for the damping coefficients of the same MREs in the absence of a magnetic field. Hence, as amplitude ratios are increased, the damping ratio approaches that of the non-field damping ratio.

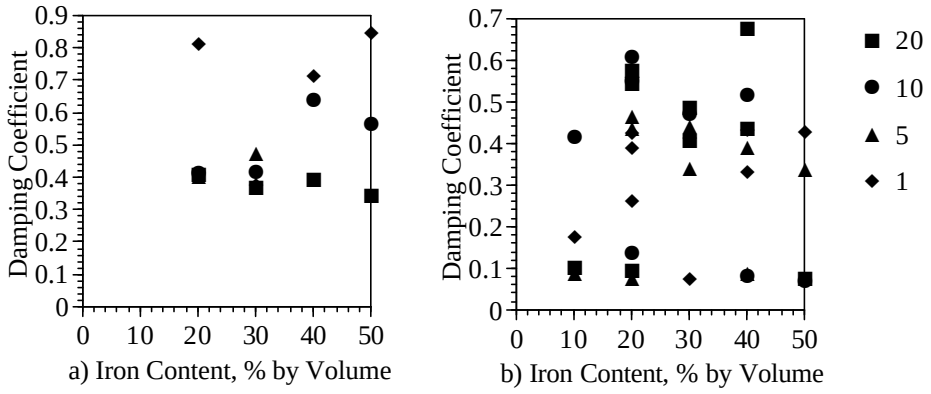

Figure 7.2: Damping ratios for a) long and b)short chain MREs in the presence of magnetic fields.

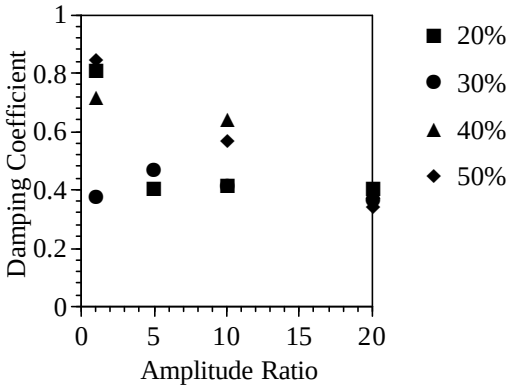

Figure 7.3: Damping ratio versus amplitude ratio for long-chain MREs of different iron content.

The fact that all the long-chain MREs have damping ratios whose characteristics approach that of the non-field damping ratios in high amplitude excitation is unsurprising. Since the magnetic field was modeled in this work as a zeroth-order force, any excitation

that takes the MRE outside the neighborhood of action of that force would be similar to the lack of force. In other words, for high excitation levels, the MRE spends more time where all particles are completely separated and not under chain influence, just as if it were not under the influence of a magnetic field. The only difference is a small static force applied under those circumstances, which would not affect the damping ratio.

7.3 The effect of static displacement on damping coefficients

Because most longitudinal mode SSAs place MREs in some sort of static displacement condition, static displacements were simulated to find the effect on damping ratios. Figure 7.4 shows damping ratios for MREs at static displacement ratios varying between -1 and 1, where 0 is an undeformed MRE. Figure 7.4a shows damping ratios in the absence of a magnetic field, and Figure 7.4b shows damping ratios of the same MREs in the presence of a magnetic field. While there is no discernable pattern between the different static displacement levels, the variation between damping ratios when the magnetic field is on is nearly double that of when the magnetic field off. This leads to the conclusion that when a magnetic field is present, damping ratios are more variable by iron content and static displacement conditions than if the magnetic field is absent.

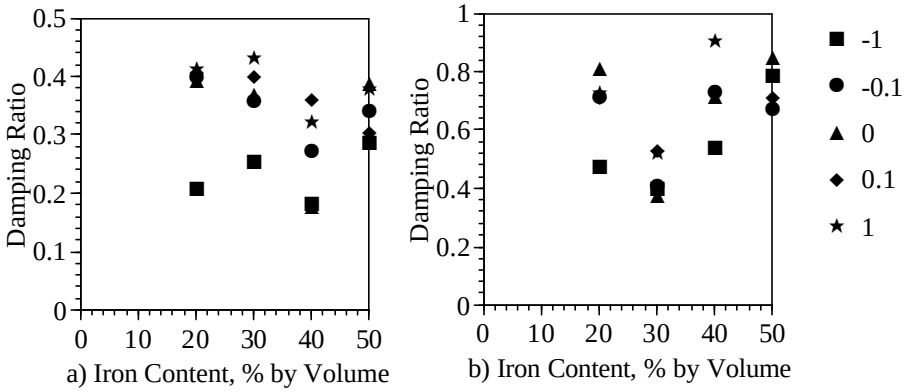

Figure 7.4: Damping ratios versus MRE content for long-chain MREs when magnetic fields are a) off and b) on at different static displacement levels.

CHAPTER VIII

DISCUSSION OF SIGNIFICANT FINDINGS

The purpose of this work was to assess the transient behavior of MREs in order to better utilize them in SSA applications. To that end, numerical and experimental studies were conducted to determine the interdependencies of outputs such as loss factor, natural frequency, and CRTs on inputs such as MRE iron content, magnetic field strength, and static displacement. Of particular significance, and benefit to the engineering community, are that

- A model was developed that combines elastomer and ferromagnetic properties to synthesize model MREs.
- This model is mass-normalized, and scales up appropriately.
- The model validates experimental findings that MRE natural frequency increases in the presence of magnetic fields for long-chain MREs.
- Damping coefficients in simulation results were found to be largely insensitive to parameter changes, and thus validated as not the mechanism for frequency change in MREs
- CRTs are longer when a magnetic field was turned on than off, for both simulation and experimental results. There was no MRE content dependency nor amplitude dependency.
- CRTs are insensitive to magnetic field strength, which means that open-loop input shaping control may not be used to control CRT behavior.

The significance of these findings are discussed in the following sections.

8.1 Model Development

A numerical model was developed that combines pure elastomer properties with ferromagnetic properties to simulate an MRE. Prior to this model being developed, MRE properties were homogenized before running an FEM/FEA analysis. While this model is in its unrefined stages, it has been validated that the model simulates a frequency increase when subjected to a magnetic field, and natural frequency results are robust when the model is scaled up, and thus holds for any size MRE, so long as the simulation dimensions are proportional to the MRE dimensions of interest. This represents a significant advantage to those in MRE research, as this model affords the opportunity to simulate different MRE formulations without first having to create the MREs.

8.2 Natural Frequency versus Static Displacement

Repeatability has been a limiting factor in MRE experimentation, development, and adaptation into the commercial world. The research presented here provides evidence that geometric constraints as well as static forcing conditions can adversely affect an MRE's ability to shift natural frequencies in a magnetic field. The numerical simulation performed for this dissertation showed that iron particle chains must be in contact in order to yield positive natural frequency shifts. This was confirmed by experimental results, both in the inability to yield a natural frequency shift using methodologies discussed in Chapter IV, but also by examining the successful shifts in a squeeze-mode vibration absorber. The squeeze-mode vibration absorber conformed to this static displacement requirement if the static displacement was measured in reference to neighboring particle proximity; it actually speaks to the need to allow MREs to be free to change geometry to accommodate neighboring particles.

8.3 Characteristic Response Times versus Magnetic Fields

CRTs are critical to SSA applications because an SSA that does not shift in less than a 1/4-period risks instability. It was determined that CRTs are sensitive to the nature of the changing magnetic field. That is to say, CRTs are larger if a magnetic field was turned on

than if it was turned off. CRTs depend on the amount of iron present in the MRE, but are unaffected by amplitude and magnetic field levels. Both of these findings were determined both experimentally and simulated numerically. Because MREs exposed to a magnetic field turning off respond more slowly than MREs in fields turning on, input shaping control is more desired for when a magnetic field turns off.

Unfortunately, CRTs are insensitive to the baseline magnetic field level. This means that a CRT can not be decreased by increasing the magnetic field beyond what is desired and then bringing it back down to the appropriate levels. This means that input shaping would not be valid for MREs, which could affect their abilities to function as commercially-available SSAs.

More work must be conducted to conclusively decide MREs' effectiveness as variable springs in SSAs, but this work represents a major step forward in that MRE mechanics are better understood. It has been confirmed that loss factors are not affected by magnetic fields, and the importance of static displacement and its role in natural frequency shifts is known, and bounds have been placed on the CRT for magnetic fields.

8.4 Damping Coefficient Dependencies

Damping coefficients are typically identified from experimental data as a system property, and at each different magnetic field level, the best-fit damping coefficient is identified. The results of this work demonstrate that damping coefficients are generally independent of geometric properties. This means that compressing or stretching an MRE does not change the damping coefficient. The engineering community has long modeled MREs as variable-stiffness springs in the presence of magnetic fields. From this work it can be concluded that MREs are indeed variable-stiffness springs, and that damping coefficients, while affected by the magnetic field, are not the material driving force behind the materials' behavior change.

CHAPTER IX

FUTURE WORK

The work presented in this dissertation represents a proof-of-concept of the underlying principles that drives stiffness changes in MREs when they are excited longitudinally. Using only zeroth-order magnetic field effects, this model was able to demonstrate stiffness increases as a function of iron content that was consistent with known experimental results. Furthermore, transient characteristic response time was consistent with experimental data. This work also exposes further unknown and unexplored areas that would represent significant leaps in future scientific understanding.

While there were several significant findings, here there were several numerical simulations from which no conclusions could be drawn. In this chapter, ideas for future refinement of this model, specifically to address these short-comings, are developed. Topics for future work that are discussed here are more sophisticated models for the elastomeric host, inlclusion of transverse neighboring particle bonds, modeling higher-order magnetic field effects, and reexamining the chain break algorithm.

9.1 Elastomeric Host Modeling

The elastomer was modeled in this work as a linear spring and damper. The results yielded FSRs and CRTs that were similar in character to those observed experimentally. However, the similarities disappeared when the effects of static displacement and amplitude variation were examined. One of the likely causes of these discrepancies is the linear spring modeled for the elastomeric host.

The linear modeling of an elastomer, as used in this work, is only valid for small elastomeric displacement. However, the deformations within the simulated matrix are not small with respect to the individual node-sizes of elastomer. Therefore, the effect of the geometric distortion, lamination, etc. should be a significant contribution to the MRE's

overall behavior. This would particularly affect any static displacement behavior and and amplitude variations.

When an MRE is subjected to a nonzero static displacement in addition to dynamic excitation, the effect of secondary deformation has an effect on the perceived Young's modulus.

9.2 Neighboring Bond Modeling

For this work, all particles were separated by elastomer material in the transverse direction. That meant that there was no possibility for particle-to-particle magnetic bonds of separate chains. However, Figure 2.2 showns particle chains that twist together and interrelate. Furthermore, results from Section 5.1 demonstrated that long-chain MREs more accurately reflect true MRE behavior than short-chain MREs. In addition, MREs that lacked contiguous chain-to-chain relationships related even less to MRE behavior than their contiguous chain-to-chain counterparts. It is the belief of this author that the inclusion of chain-to-chain magnetic field modeling would amend the discrepancy between these two classes of simulated MREs.

9.3 Inclusion of Higher-Order Magnetic Field Terms

In Section 3.1, the attractive force between two particles was shown to be inversely proportional to the square of the separation distance. In this work, the magnetic force has been simplified to its zeroth-order component, where the nominal displacement is assumed to be the one that allows for a static equilibrium. However, higher-order terms are present and can be significant to MRE performance. It is proposed that future work examines the effects of these higher-order terms on simulated MRE performance.

The reason for this is that the first-order approximation of a magnetic field is known to serve as a softening-spring effect [30]. These first-order approximations undermine the stiffening effect found in the zeroth-order approximation studied in this work. What will be particularly compelling and informative is a study of the interactions between excitation

amplitude and inclusion of first-order effects. Since higher-order effects are more significant than lower-order effects with additional amplitude, it is suspected that first-order approximations will impact the amplitude studies more than any other phenomenon.

9.4 Integration of MRE Dynamics and SSA Algorithm

It was found that there is a differential CRT for MREs when a magnetic field is turned on versus when it is turned off. This means that when applying an MRE in an open-loop control system such as an SSA algorithm, it may be necessary to employ input shaping on the magnetic field. Input shaping would serve to generate desirable MRE behavior from the outset and to minimize transients.

9.5 Chain Break by Force Analysis

In order to conduct this research, chain breaks were found through an iterative process using a static balance. That is to say, a static strain was applied to the simulated MRE with all chains intact. The chain chosen to break first was the chain experiencing the largest force gradient, and within the chain, the particular bond that broke was the one experiencing the largest force gradient. That particular bond break was assumed hereonafter to always be the first bond to break, and would break when the absorber mass's displacement relative to the base mass exceeded the pre-established change in displacement. Subsequent chain breaks were calculated in an iterative manner, and once all chain breaks were found, the order of breaks were assumed to stay constant.

This is a valid assumption if only the lowest few modes of the system are activated. At higher modes, the order of quasi-static bond breaking is no longer indicative of the order of chain breaking. Instead, at each time step the forces applied to each bond must be compared to the magnetic attractive force. This would lead to greater accuracy in numerical predictions of MRE behavior at higher frequencies.

CHAPTER X

CONCLUSIONS

The purpose of this work was to better understand the mechanics of MRE behavior so that they may be implemented as springs in SSA devices. Numerical simulations were created from numerical models of iron-iron interactions and mass-spring mechanics. These simulations results were validated with experimental data. The main focus of this work was the assessment of damping coefficients, natural frequencies, and transient times, and how each of these properties were affected by forcing frequency and amplitude, static displacement, and iron content and configuration.

Simulations were run in Matlab rather than FEA software because MREs were modeled as elastomer-iron matrices rather than a homogenous material with magnetic properties. Damping coefficients were evaluated and determined to be independent of parameters such as static displacement and amplitude of excitation. This was a significant finding because it confirms that changes in MRE natural frequency are due to stiffness changes as opposed to damping variance.

Long-chain MREs were found to best represent the experimental MRE behavior, as they exhibited natural frequency increases at the appropriate iron content value. Furthermore, large amplitude excitation decreased the MREs' FSR. This matches experimental results, and makes sense within the context of the known theory governing MRE behavior.

Transient behavior was assessed by finding a characteristic response time rather than a rise or settling time because MREs are constantly exposed to internal transients within the context of chain breaks. CRTs were determined by looking at quasi-steady state behavior, and measuring the time it took to achieve that behavior. CRT was correlated to forcing frequencies, and CRT was found to be insensitive to the magnitude of the applied magnetic field.

CRTs varied depending on whether the MRE was exposed to a magnetic field being

turned on or off. Both numerical and experimental results showed that CRTs were longer when an MRE was exposed to a magnetic field turning off than when the magnetic field turned on. This is because when an MRE is exposed to a magnetic field that is just turned off, chain formation are limited by particle dynamics, whereas chains are forced into the appropriate behavior when a magnetic field is turned on. This is a significant finding because the limitations of MREs is exposed. The dynamics of the MREs, when the magnetic field is turned off, are unaffected by magnetic field strength and hence not controllable using open-loop input shaping of the magnetic field. However, possibilities for small amounts of magnetic field in the opposite direction have not been studied nor ruled out as a possibility for affecting this behavior.

Using both numerical and empirical results, transient behavior of MREs was assessed. The relationship between natural frequency, damping, static displacement, CRT, and magnetic field were determined. This work allows future researchers to assess the controllability of MRE transient behavior, and shape it appropriately for SSA use.

REFERENCES

[1] Abe, M. and Igusa, T., "Semi-active dynamic vibration absorbers for controlling transient response," *Journal of Sound and Vibration*, vol. 198, no. 5, pp. 547–569, 1996.

[2] Albanese, A. M. and Cunefare, K. A., "Properties of a magnetorheological semi-active vibration absorber," in *SPIE*, vol. 5052 of *Smart Structures and Materials 2003: Damping and Isolation*, (San Diego, California, USA), pp. 36–43, 2003.

[3] Bay, J. S., *Fundamentals of Linear State Space Systems*. Boston: McGraw-Hill, 1999.

[4] Bednarek, S., "Susceptibility of magnetodielectrics within an elastomer matrix to length changes in heterogeneous magnetic field," *Applied Physics A (Materials Science Processing)*, vol. 66, no. 6, pp. 643–650, 1998.

[5] Bednarek, S., "The giant magnetostriction in ferromagnetic composites within an elastomer matrix," *Applied Physics A (Materials Science Processing)*, vol. 68, no. 1, pp. 63–67, 1999.

[6] Bellan, C. and Bossis, G., "Field dependence of viscoelastic properties of mr elastomers," *Internation Journal of Modern Physics B*, vol. 16, no. 17-18, pp. 2447–2453, 2002.

[7] Bossis, G., Abbo, C., Cutillas, S., Lacis, S., and Metayer, C., "Electroactive and electrostructured elastomers," *International Journal of Modern Physics B*, vol. 15, no. 6-7, pp. 564–73, 1999.

[8] Brigadnov, I. A. and Dorfmann, A., "Mathematical modeling of magneto-sensitive elastomers," *International Journal of Solids and Structures*, vol. 40, no. 18, pp. 4659–4674, 2003.

[9] Cunefare, K. A., DeRosa, S., Sadegh, N., and Larson, G., "State-switched absorber for semi-active structural control," *Journal of Intelligent Material Systems and Structures*, vol. 11, no. 4, pp. 300–310, 2000.

[10] Davis, L. C., "Model of magnetorheological elastomers," *Journal of Applied Physics*, vol. 85, no. 6, pp. 3348–3351, 1999.

[11] Den Hartog, J. P., *Mechanical Vibrations*. New York: reprinted by Dover, 1956.

[12] Farshad, M. and Benine, A., "Magnetoactive elastomer composites," *Polymer Testing*, vol. 23, no. 3, pp. 347–353, 2004.

[13] Frahm, H., "Device for damping vibration of bodies," U.S. patent no. 989958, April 18 1911.

[14] Ginder, J. M., "Rheology controlled by magnetic fields," in *Encyclopedia of applied physics* (Trigg, G. L., Vera, E. S., and Greulich, W., eds.), vol. 16, pp. 487–503, New York, NY: VCH Publishers, 1991.

[15] Ginder, J. M., Clark, S. M., Schlotter, W. F., and Nichols, M. E., "Magnetostrictive phenomena in magnetorheological elastomers," *International Journal of Modern Physics B*, vol. 16, no. 17-18, pp. 2412–2418, 2002.

[16] Ginder, J. M., Davis, L. C., and Elie, L. D., "Rheology of magnetorheological fluids: models and measurements technology," *International Journal of Modern Physics B*, vol. 10, no. 23-24, pp. 3293–3303, 1996.

[17] Ginder, J. M., Nichols, M. E., Elie, L. D., and Tardiff, J. L., "Magnetorheological elastomers: properties and applications," in *SPIE Conference on Smart Materials Technologies*, vol. 3675, (Newport Beach, CA), pp. 131–138, 1999.

[18] Guth, E., "Theory of filler reinforcement," *Journal of Applied Physics*, vol. 16, no. 20, pp. 20–25, 1945.

[19] Hayt, J., W. H. and Buck, J. A., *Engineering Electromagnetics*. Boston: McGraw-Hill, 6th ed., 2001.

[20] Holdhusen, M. and Cunefare, K. A., "Damping effects on the state-switched absorber used for vibration suppression," *Journal of Intelligent Material Systems and Structures*, vol. 14, no. 9, pp. 551–561, 2003.

[21] Holdhusen, M. and Cunefare, K. A., "Optimization of location and tuning of a state-switched absorber for controlling beam vibration," in *SPIE*, vol. 5049, (San Diego, California, USA), pp. 404–413, 2003.

[22] Jolly, M. R., Carlson, J. D., and Munoz, B. C., "Model of the behaviour of magnetorheological materials," *Smart Materials and Structures*, vol. 5, no. 5, pp. 607–614, 1996.

[23] Jolly, M. R., Carlson, J. D., Munoz, B. C., and Bullions, T. A., "The magnetoviscoelastic response of elastomer composites consisting of ferrous particles embedded in a polymer matrix," *Journal of Intelligent Material Systems and Structures*, vol. 7, no. November, pp. 613–622, 1996.

[24] Karnopp, D., Crosby, M. J., and Harwood, R. A., "Vibration control using semi-active force generators," *Journal of Engineering for Industry*, vol. 96, no. series B, no.2, pp. 619–626, 1974.

[25] Lerner, A. A., *The Design and Implementation of a Magnetorheological Silicone Composite State-Switched Absorber*. PhD thesis, Georgia Institute of Technology, 2004.

[26] Lerner, A. A. and Cunefare, K. A., "Performance of mre-based vibration absorbers," *JIMSS*, vol. 5, no. OnlineFirst: 1045389X07077850, 2007.

[27] Meinecke, E. A. and Taftaf, M. I., "Effect of carbon black on the mechanical properties of elastomers," *Rubber Chemistry and Technology*, vol. 61, no. 3, pp. 534–547, 1988.

[28] Meirovitch, L., *Elements of vibration analysis*. New York: McGraw Hill, 2nd ed., 1986.

[29] Morison, J. and Karnopp, D., "Comparison of optimized active and passive vibration absorbers," *American Automatic Control Council*, vol. 35, no. 2, pp. 932–938, 1973.

[30] Piombo, B. A. D., Vigliani, A., and Bonisoli, E., "Dynamics of suspensions with rare-earth permanent magnets," in *SPIE*, vol. 5052 of *Smart Structures and Materials 2003*, (San Diego, California, USA), 2003.

[31] Rigbi, Z. and Jilken, L., "The response of an elastomer filled with soft ferrite to mechanical and magnetic influences," *Journal of Magnetism and Magnetic Materials*, vol. 37, pp. 267–276, 1983.

[32] Shiga, T., Ohta, T., Hirose, Y., Okada, A., and Kurauchi, T., "Electroviscoelastic effect of polymeric composites consisting of polyelectrolyte particles and polymer gel," *Journal of Materials Science*, vol. 28, pp. 1293–1299, 1993.

[33] Shiga, T., Okada, A., and Kurauchi, T., "Magnetroviscoelastic behavior of composite gels," *Journal of Applied Polymer Science*, vol. 58, no. 4, pp. 787–792, 1995.

[34] Shkel, Y. M. and Klingenberg, D. J., "Magnetorheology and magnetostriction of isolated chains of nonlinear magnetizable spheres," *Journal of Rheology*, vol. 45, no. 2, pp. 351–368, 2001.

[35] Sun, J. Q., Jolly, M., and Norris, M., "Passive, adaptive, and active tuned vibration absorbers-a survey," *Journal of Vibration and Acoustics*, vol. 177, no. 3B, pp. 234–42, 1995.

[36] Sun, L. Z., Yin, H. M., and Chen, J. S., "Micromechanics-based hyperelastic constitutive modeling of magnetostrictive particle-filled elastomers," *Mechanics of Materials*, vol. 34, no. 8, pp. 505–516, 2002.

[37] Todaka, T., Enokizono, M., Fujita, E., and Ogura, Y., "Moving simulation of vibration systems using permanent magnets," *IEEE Transactions on Magnetics*, vol. 37, no. 5, pp. 3456–3459, 2001.

[38] Watson, J. R., "Method and apparatus for varying the stiffness of a suspension bushing," March 11,1997 1997.

[39] Yu, Z., Meng, L. T., and King, L. M., "Electromagnetic bearing actuator for active vibration control of a flexible rotor," *Journal of Mechanical Engineering Science*, vol. 212, no. 8, pp. 705–716, 1998.

[40] Zhou, G. Y., "Shear properties of a magnetorheological elastomer," *Smart Materials and Structures*, vol. 12, pp. 139–146, 2003.

[41] Zhou, G. Y., "Complex shear modulus of a magnetorheological elastomer," *Smart Materials and Structures*, vol. 13, pp. 1203–1210, 2004.

[42] Zhou, G. Y. and Jiang, Z. Y., "Deformation in magnetorheological elastomer and elastomer-ferromagnet composite driven by a magnetic field," *Smart Materials and Structures*, vol. 13, no. 2, pp. 309–316, 2004.

[43] Zhou, G. Y. and Li, J. R., "Dynamic behavior of a magnetorheological elastomer under uniaxial deformation: I. experiment," *Smart Materials and Structures*, vol. 12, no. 6, pp. 859–872, 2003.

APPENDIX A

NUMERICAL MRE SAMPLES

MRE micro-samples consisted of thirty nodes; each node was assigned either a value of "spring", labelled as a "0", or "particle", labeled as a "1". Each sample was in either a 6×5 or 5×6 configuration. The samples used were configured as follows:

10% MREa, short:

$$\begin{bmatrix} 0 & 0 & 1 & 0 & 0 \\ 0 & 0 & 1 & 0 & 0 \\ 0 & 0 & 1 & 0 & 0 \\ 0 & 0 & 0 & 0 & 0 \\ 0 & 0 & 0 & 0 & 0 \\ 0 & 0 & 0 & 0 & 0 \end{bmatrix}$$

20% MREa, long:

$$\begin{bmatrix} 0 & 0 & 1 & 0 & 0 \\ 0 & 0 & 1 & 0 & 0 \\ 0 & 0 & 1 & 0 & 0 \\ 0 & 0 & 1 & 0 & 0 \\ 0 & 0 & 1 & 0 & 0 \\ 0 & 0 & 1 & 0 & 0 \end{bmatrix}$$

20% MREb, short:

$$\begin{bmatrix} 0 & 1 & 0 & 0 & 0 \\ 0 & 1 & 0 & 0 & 0 \\ 0 & 1 & 0 & 0 & 0 \\ 0 & 0 & 1 & 0 & 0 \\ 0 & 0 & 1 & 0 & 0 \\ 0 & 0 & 1 & 0 & 0 \end{bmatrix}$$

20% MREc, short:

$$\begin{bmatrix} 0 & 1 & 0 & 0 & 0 & 0 \\ 0 & 1 & 0 & 0 & 0 & 0 \\ 0 & 1 & 0 & 0 & 1 & 0 \\ 0 & 0 & 0 & 0 & 1 & 0 \\ 0 & 0 & 0 & 0 & 1 & 0 \end{bmatrix}$$

20% MREd, short:

$$\begin{bmatrix} 0 & 1 & 0 & 0 & 0 \\ 0 & 1 & 0 & 0 & 0 \\ 0 & 0 & 1 & 0 & 0 \\ 0 & 0 & 1 & 0 & 0 \\ 0 & 0 & 0 & 1 & 0 \\ 0 & 0 & 0 & 1 & 0 \end{bmatrix}$$

30% MREa, long:

$$\begin{bmatrix} 0 & 0 & 1 & 1 & 0 & 0 \\ 0 & 0 & 1 & 1 & 0 & 0 \\ 0 & 0 & 1 & 1 & 0 & 0 \\ 0 & 0 & 1 & 1 & 0 & 0 \\ 0 & 0 & 1 & 1 & 0 & 0 \end{bmatrix}$$

30% MREb, short:

$$\begin{bmatrix} 0 & 1 & 0 & 0 & 0 & 0 \\ 0 & 1 & 0 & 1 & 0 & 0 \\ 0 & 1 & 0 & 1 & 0 & 1 \\ 0 & 0 & 0 & 1 & 0 & 1 \\ 0 & 0 & 0 & 0 & 0 & 1 \end{bmatrix}$$

30% MREc, short:

$$\begin{bmatrix} 0 & 0 & 1 & 0 & 0 \\ 0 & 0 & 1 & 1 & 0 \\ 0 & 0 & 1 & 1 & 0 \\ 0 & 1 & 0 & 1 & 0 \\ 0 & 1 & 0 & 1 & 0 \\ 0 & 1 & 0 & 0 & 0 \end{bmatrix}$$

40% MREa, long:

$$\begin{bmatrix} 0 & 1 & 0 & 1 & 0 \\ 0 & 1 & 0 & 1 & 0 \\ 0 & 1 & 0 & 1 & 0 \\ 0 & 1 & 0 & 1 & 0 \\ 0 & 1 & 0 & 1 & 0 \\ 0 & 1 & 0 & 1 & 0 \end{bmatrix}$$

40% MREb, short:

$$\begin{bmatrix} 0 & 0 & 1 & 0 & 0 & 1 \\ 0 & 0 & 1 & 0 & 0 & 1 \\ 0 & 1 & 0 & 0 & 1 & 0 \\ 0 & 1 & 1 & 1 & 1 & 0 \\ 0 & 0 & 1 & 1 & 0 & 0 \end{bmatrix}$$

40% MREc, short:

$$\begin{bmatrix} 0 & 0 & 1 & 0 & 0 & 1 \\ 0 & 0 & 0 & 1 & 0 & 1 \\ 1 & 0 & 1 & 1 & 0 & 1 \\ 1 & 0 & 1 & 0 & 0 & 0 \\ 1 & 0 & 1 & 0 & 0 & 0 \end{bmatrix}$$

50% MREa, long:

$$\begin{bmatrix} 0 & 1 & 1 & 0 & 1 & 0 \\ 0 & 1 & 1 & 0 & 1 & 0 \\ 0 & 1 & 1 & 0 & 1 & 0 \\ 0 & 1 & 1 & 0 & 1 & 0 \\ 0 & 1 & 1 & 0 & 1 & 0 \end{bmatrix}$$

50% MREb, short:

$$\begin{bmatrix} 0 & 1 & 1 & 0 & 1 & 0 \\ 0 & 1 & 1 & 0 & 1 & 0 \\ 0 & 1 & 0 & 1 & 1 & 0 \\ 1 & 0 & 0 & 1 & 0 & 1 \\ 1 & 0 & 0 & 1 & 0 & 1 \end{bmatrix}$$

APPENDIX B

SQUEEZE-MODE VIBRATION ABSORBER EXPERIMENTAL METHOD

Figure B.1 is a schematic of the apparatus used to obtain experimental results for a squeeze-mode vibration absorber. A magnetic field was delivered by attaching the wire coil ends to a KEPCO model 36-6D power supply, which supplied up to 6 A of direct current. For experiments requiring device excitation, a data acquisition system was used to generate a white noise signal, low-pass filtered to 1000 Hz. This signal was amplified by an LDS PA25E power amplifier, and excited the base mass using an LDS V205 shaker. The shaker was rigidly attached to the base mass.

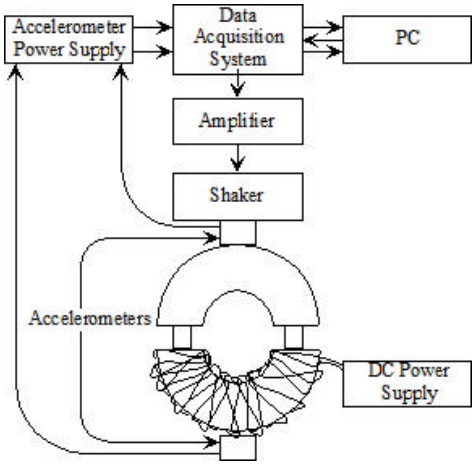

Figure B.1: A squeeze-mode vibration absorber is depicted with its experimental setup.

Data in the form of magnetic field, displacement, and acceleration were collected to determine device characteristics. Magnetic fields were measured by a Lakeshore model 480 fluxmeter, using a sensor with 125 turns of wire. The fluxmeter probe could be placed around the base mass, as indicated by Figure B.1, or around the MREs. Acceleration data was collected by a PCB 303A02 accelerometer, attached to the absorber mass, and a PCB

288A11 accelerometer, which was attached to the base mass. Information that was static in nature, such as the static displacement of the absorber mass, was measured using a Philtec model D100-QPT displacement probe. The displacement probe was located such that it could measure the absolute displacement of the absorber mass. Data from accelerometers and the displacement probe were acquired by a Siglab model 50-21 data acquisition system, and then transferred to a PC.

MREs were placed in a squeeze mode vibration absorber configuration and the base mass was subjected to white noise, band limited at 1000 Hz. Acceleration data was collected from the base mass and the absorber mass. The MRE was modeled as a spring with complex stiffness, having a loss factor δ and stiffness K. The equation of motion governing the system was assumed to be

$$M\ddot{x}_{abs} + Ke^{i\delta}x_{abs} = Ke^{i\delta}x_{base}, \tag{B.1}$$

where M was the absorber mass, . An FFT was applied to the data, yielding a transfer function

$$H(\omega) = \frac{X_{abs}(\omega)}{X_{base}(\omega)} = \frac{Ke^{i\delta}}{Ke^{i\delta} - \omega^2 M} = \frac{\omega_n^4 - \omega^2\omega_n^2\cos\delta - i\omega^2\omega_n^2\sin\delta}{\omega_n^4 + \omega^4 - 2\omega^2\omega_n^2\cos\delta}, \tag{B.2}$$

where $\omega_n^2 = \frac{K}{M}$. The phase angle and amplitude of Equation B.2 were found and analyzed to empirically determine the values of ω_n and δ for each data set. The phase angle between the absorber and base masses may be written as

$$\angle H(\omega) = \tan^{-1}\left(\frac{\omega^2\sin\delta}{\omega^2\sin\delta - \omega_n^2}\right). \tag{B.3}$$

Using Equation B.3, the phase angle can be shown to cross -90° when

$$\omega = \omega_{90^\circ} = \frac{\omega_n}{\sqrt{\cos\delta}}. \tag{B.4}$$

Substituting this into Equation B.2, the amplitude can be found to be

$$|H(\omega)| = \frac{\omega_{90^\circ}^2\cos\delta}{\left[\omega^4 + \omega_{90^\circ}^4\cos^2\delta - 2\omega^2\omega_{90^\circ}^2\cos\delta\right]^{1/2}}. \tag{B.5}$$

The natural frequency, ω_n, and loss factor, δ, were found by first identifying ω_{90° from the phase angle data. Amplitude data was calculated using Equation B.5, where $\delta = \frac{n\pi}{40}$,

$n = 1, 2, \ldots 20$. The δ value was selected when

$$\frac{\partial\left(e^2\right)}{\partial\delta} = 2e\frac{\partial e}{\partial\delta} = 2\sum_{m=1}^{M}\left[\left(\left|y\left(\omega_m\right)\right| - \left|H\left(\omega_m, \delta_n\right)\right|\right)\cdot\left(-\frac{\partial\left|H\left(\omega_m, \delta_n\right)\right|}{\partial\delta_n}\right)\right] = 0, \tag{B.6}$$

where $y\left(\omega_m\right)$ was the experimental data value at frequency ω_m. Equation B.6 finds the point of zero-slope in the squared-error curve. This indicated points of maximum and minimum error. Since

$$\frac{\partial\left|H\left(\omega, \delta\right)\right|}{\partial\delta} = \frac{-\omega_{90^\circ}^2\omega^4\sin\delta}{\left[\omega^4 + -\omega_{90^\circ}^4\cos^2\delta - 2\omega_{90^\circ}^2\omega^2\cos\delta\right]^{3/2}}, \tag{B.7}$$

values at $\delta = 0$ were ignored. Once a δ-value had been ascertained, the natural frequency, ω_n, was determined by substituting δ back into Equation B.4.

APPENDIX C

CHARACTERISTIC RESPONSE TIMES VERSUS MAGNETIC FIELD RATIOS

MREs described in Appendix A were subjected to magnetic field ratios of 1, 0.75, 0.5, and 0.25, where a magnetic field ratio was the ratio of the applied magnetic field to the magnetic field that would cause total saturation of the magnetic particles. Data points were omitted if the simulation yielded numerical instability.

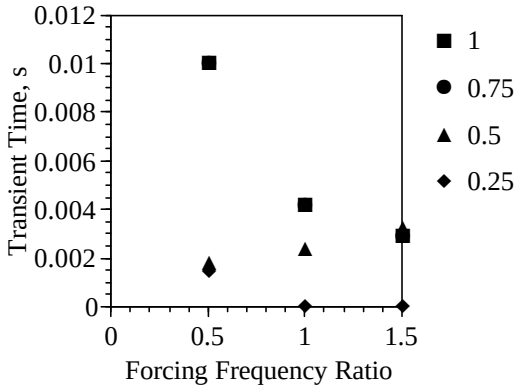

Figure C.1: CRT is plotted against forcing frequency ratios at magnetic field ratios of 1, 0.75, 0.5, and 0.25 for MRE 10a.

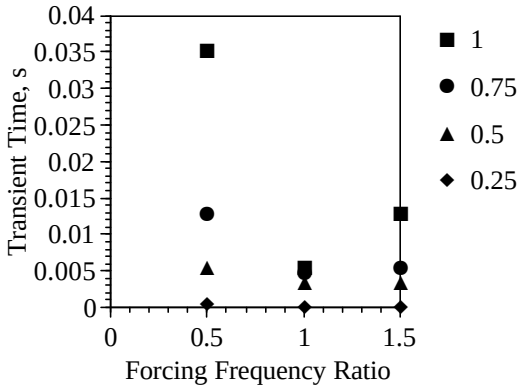

Figure C.2: CRT is plotted against forcing frequency ratios at magnetic field ratios of 1, 0.75, 0.5, and 0.25 for MRE 20a.

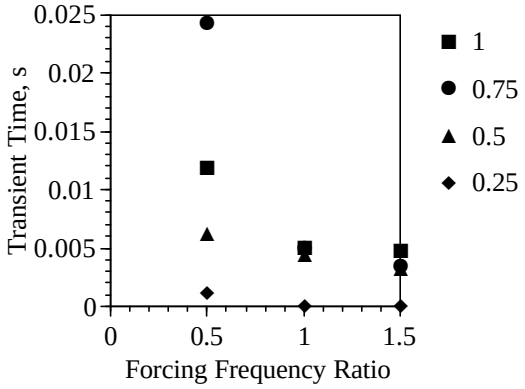

Figure C.3: CRT is plotted against forcing frequency ratios at magnetic field ratios of 1, 0.75, 0.5, and 0.25 for MRE 20b.

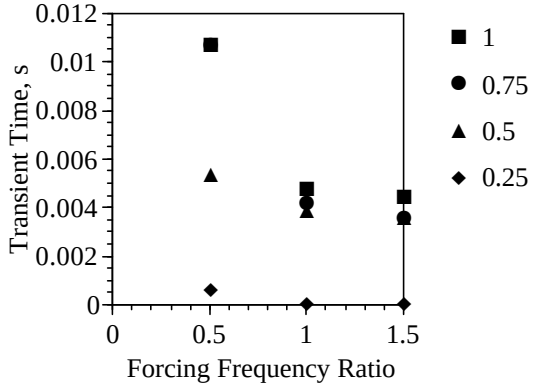

Figure C.4: CRT is plotted against forcing frequency ratios at magnetic field ratios of 1, 0.75, 0.5, and 0.25 for MRE 20c.

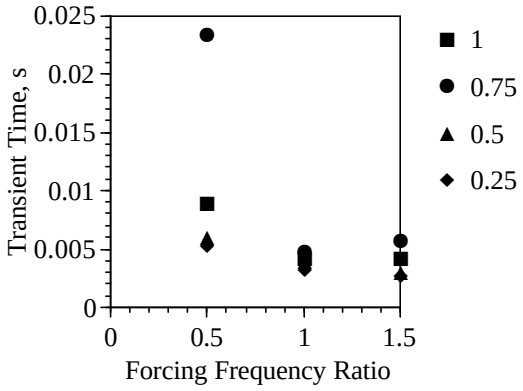

Figure C.5: CRT is plotted against forcing frequency ratios at magnetic field ratios of 1, 0.75, 0.5, and 0.25 for MRE 20d.

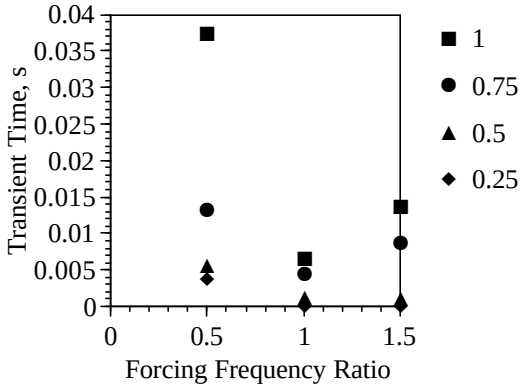

Figure C.6: CRT is plotted against forcing frequency ratios at magnetic field ratios of 1, 0.75, 0.5, and 0.25 for MRE 30a.

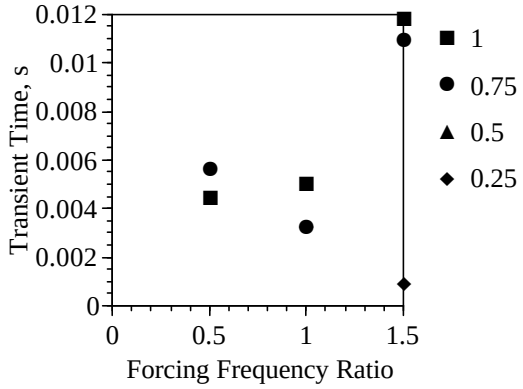

Figure C.7: CRT is plotted against forcing frequency ratios at magnetic field ratios of 1, 0.75, 0.5, and 0.25 for MRE 30b.

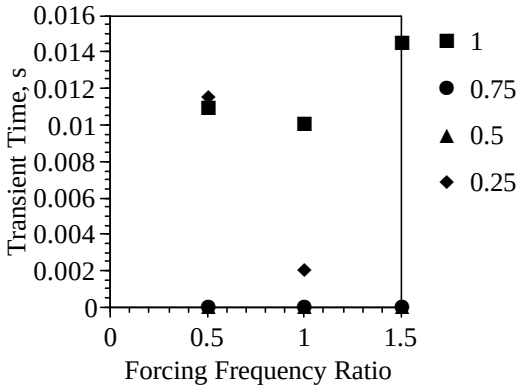

Figure C.8: CRT is plotted against forcing frequency ratios at magnetic field ratios of 1, 0.75, 0.5, and 0.25 for MRE 30c.

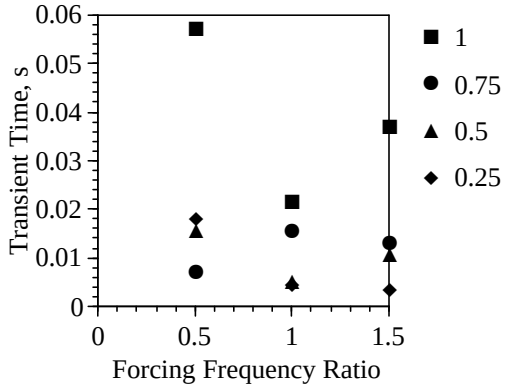

Figure C.9: CRT is plotted against forcing frequency ratios at magnetic field ratios of 1, 0.75, 0.5, and 0.25 for MRE 40a.

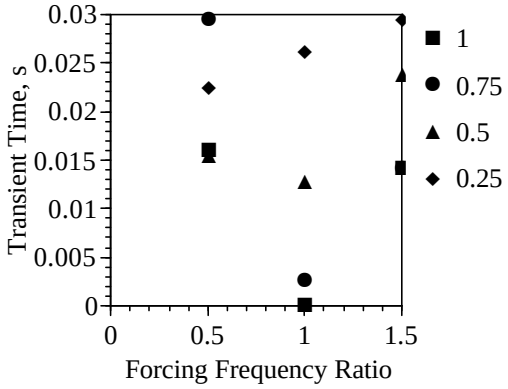

Figure C.10: CRT is plotted against forcing frequency ratios at magnetic field ratios of 1, 0.75, 0.5, and 0.25 for MRE 40b.

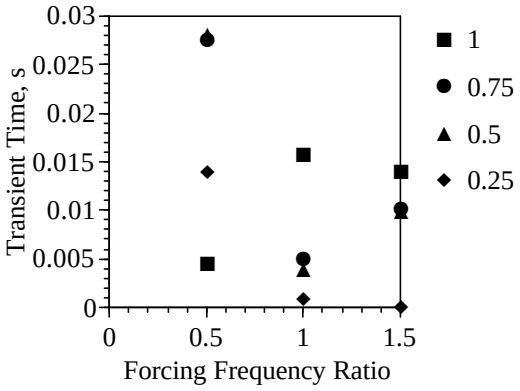

Figure C.11: CRT is plotted against forcing frequency ratios at magnetic field ratios of 1, 0.75, 0.5, and 0.25 for MRE 40c.

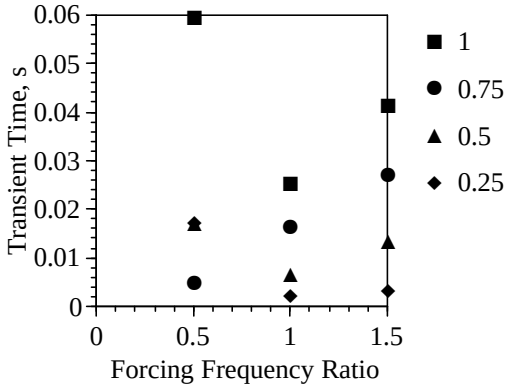

Figure C.12: CRT is plotted against forcing frequency ratios at magnetic field ratios of 1, 0.75, 0.5, and 0.25 for MRE 50a.

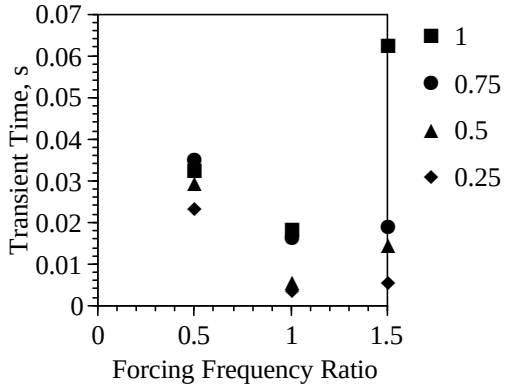

Figure C.13: CRT is plotted against forcing frequency ratios at magnetic field ratios of 1, 0.75, 0.5, and 0.25 for MRE 50b.